

# Decoupling of Magnetic Fields in Collapsing Protostellar Envelopes and Disc Formation and Fragmentation

Bo Zhao<sup>1</sup><sup>\*</sup><sup>†</sup>, Paola Caselli<sup>1</sup>, Zhi-Yun Li<sup>2</sup>, Ruben Krasnopolsky<sup>3</sup>

<sup>1</sup>Max-Planck-Institut für extraterrestrische Physik (MPE), Garching, Germany, 85748

<sup>2</sup>University of Virginia, Astronomy Department, Charlottesville, USA, 22904

<sup>3</sup>Academia Sinica Institute of Astronomy and Astrophysics, 10167, Taipei, Taiwan

24 September 2018

## ABSTRACT

Efficient magnetic braking is a formidable obstacle to the formation of rotationally supported discs (RSDs) around protostars in magnetized dense cores. We have previously shown, through 2D (axisymmetric) non-ideal MHD simulations, that removing very small grains (VSGs:  $\sim 10$  to few 100) can greatly enhance ambipolar diffusion and enable the formation of RSDs. Here we extend the simulations of disc formation enabled by VSG removal to 3D. We find that the key to this scenario of disc formation is that the drift velocity of the magnetic field almost cancels out the infall velocity of the neutrals in the  $10^2$ - $10^3$  AU-scale “pseudo-disc” where the field lines are most severely pinched and most of protostellar envelope mass infall occurs. As a result, the bulk neutral envelope matter can collapse without dragging much magnetic flux into the disc-forming region, which lowers the magnetic braking efficiency. We find that the initial discs enabled by VSG removal tend to be Toomre-unstable, which leads to the formation of prominent spiral structures that function as centrifugal barriers. The piling-up of infall material near the centrifugal barrier often produces dense fragments of tens of Jupiter masses, especially in cores that are not too strongly magnetized. Some fragments accrete onto the central stellar object, producing bursts in mass accretion rate. Others are longer lived, although whether they can survive long-term to produce multiple systems remains to be ascertained. Our results highlight the importance of dust grain evolution in determining the formation and properties of protostellar discs and potentially multiple systems.

**Key words:** magnetic fields -MHD- circumstellar matter - stars: formation

## 1 INTRODUCTION

Angular momentum lies in the heart of the formation of rotationally supported discs (RSDs), which is strongly affected by the magnetic flux harboured in the central disc-forming region. The winding of pinched magnetic field lines by gas rotation can cause large magnetic torques that transport angular momentum away from the equatorial region (Mestel & Spitzer 1956; Mouschovias 1977; Mouschovias & Paleologou 1980; Basu & Mouschovias 1994), preventing the formation of RSDs. This is the so-called magnetic braking problem (Allen et al. 2003; Mellon & Li 2008; Li et al. 2011), which is in tension with recent high-resolution observations of  $\sim 100$  AU discs and spirals around young protostellar objects (Tobin et al. 2012, 2013; Tokuda et al. 2014; Pérez et al. 2016; Tobin et al. 2016).

Recent theoretical studies on disc formation often resort to non-ideal MHD effects to avert the magnetic braking “catastrophe”

(Königl 1987; Mouschovias & Paleologou 1986; Mellon & Li 2009; Dapp & Basu 2010; Li et al. 2011; Krasnopolsky et al. 2011; Dapp et al. 2012; Tomida et al. 2013, 2015; Tsukamoto et al. 2015a,b; Masson et al. 2015; Wurster et al. 2016), based on the principle that magnetic fields are partially decoupled from neutral matter in weakly ionized dense cores (Bergin & Tafalla 2007). However, most studies focus on the decoupling of the magnetic field at very high densities within a few to tens of AU scale around the central star. The RSDs formed in this fashion, if any, are of limited size (at most  $\sim 30$  AU in radius) and have no clear sign of growth to the  $\sim 50$ - $100$  AU Keplerian discs observed around Class 0 protostars (Murillo et al. 2013; Codella et al. 2014; Tobin et al. 2016; Lee et al. 2017).

In our previous two-dimensional (2D) study, Zhao et al. (2016) (Zhao+16 hereafter), we have shown that large (axisymmetric) RSDs and self-gravitating rings are able to form in the absence of very small grains (VSGs) of  $\sim 10$  to few 100. In fact, it is the large population of VSGs in the MRN size distribution that dominates the coupling of the bulk neutral matter to the magnetic field at

\* Contact e-mail: bo.zhao@mpe.mpg.de

† Present address: Giessenbachstr. 1, D-85748, Garching, Germany

densities below  $10^{10} \text{ cm}^{-3}$ . The removal of VSGs can enhance the ambipolar diffusion of magnetic field in the envelope by  $\sim 1\text{--}2$  orders of magnitude, so that the amount of magnetic flux dragged by the collapse into the central disc-forming region is reduced. Because the decoupling of magnetic fields occurs much earlier, magnetic braking operating in the central equatorial region becomes inefficient in transporting away angular momentum. Therefore, the high specific angular momentum in the infalling gas eventually leads to the formation and growth of early RSDs.

According to Zhao+16, the key requirement for magnetized disc formation is the lack of VSGs in dense cores, which has been confirmed by recent CARMA centimetre survey searching for emission of spinning dust grains (Tibbs et al. 2016). They show a depletion of nanometre grains ( $\leq 100 \text{ \AA}$ ) in all dense molecular cores in their survey. The depletion of VSGs can occur either in the prestellar or protostellar phase, through both accretion of VSGs onto dust grain mantles (process analogous to molecular freeze-out, e.g., Tielens & Hagen 1982; Hasegawa et al. 1992) and grain coagulation (e.g., Chokshi et al. 1993; Dominik & Tielens 1997). Grain coagulation has been shown to be rather efficient in removing small grains ( $< 0.1 \text{ \mu m}$ ) within a few  $10^6$  years (Ossenkopf 1993; Hirashita 2012). Furthermore, the timescale for coagulation of VSGs onto big grains has shown to be the shortest ( $\sim 1.6 \times 10^3$  years; Köhler et al. 2012). Hence, prior to the birth of the protostellar disc, the collapsing envelope is likely to have a greatly reduced abundance of VSGs, which enhances ambipolar diffusion.

In this study, we extend our previous study of AD-induced disc formation to three-dimension (3D) and provide conditions for the formation of RSDs and multiple systems. We confirm the crucial role of removing VSGs in the formation of RSDs, as found in Zhao+16. Particularly, we find that the infall velocity of the magnetic field decreases to nearly zero over a wide equatorial region in the envelope, where magnetic field lines are strongly pinched by the collapsing flow. Unlike Hennebelle et al. (2016), the self-regulation of magnetic fields by AD actually occurs on much larger scales, and is due to the vertical gradient of the radial magnetic field (field pinching and the associated magnetic tension force) instead of the radial gradient of poloidal fields (and the associated magnetic pressure gradient). Efficient decoupling of magnetic fields in the envelope leads to sufficient angular momentum influx into the disc forming region, triggering the formation of an early RSD or ring ( $\sim 10\text{--}40 \text{ AU}$ ) which evolves into a small circumstellar disc ( $\sim 20 \text{ AU}$ ) surrounded by large spiral structures (a few  $100 \text{ AU}$ ). We also confirm that both rotation speed and magnetic field strength of the initial core can affect the morphology and size of the disc. For cores with lower magnetization, multiple companion objects can form from spiral or ring structures via material piling up near the centrifugal barrier, which belongs to the type of fragmentation driven by rapid accretion (Kratter et al. 2010; Kratter & Lodato 2016). The models that produce large spirals and multiple systems in 3D correspond to the models with ring structures found in the 2D axisymmetric calculations of Zhao+16.

The rest of the paper is organized as follows. Section 2 describes the initial conditions of the simulation set, together with an overview of the results. In Section 3, we present and analyse the simulation results. The comparison with existing theories of disc formation and a case study of B335 are given in Section 4. Finally, we summarize the results in Section 5.

## 2 INITIAL CONDITION

We carry out three-dimensional (3D) numerical simulations<sup>1</sup> using ZeusTW code (Krasnopolsky et al. 2010), focusing on the ambipolar diffusion for the diffusion of magnetic field in collapsing cloud cores. We adopt the same chemical network as in Zhao et al. (2016), which computes the magnetic diffusivities<sup>2</sup> at every hydrodynamic timestep and at each spatial point.

The initial conditions are similar to Zhao et al. (2016), except for a more accurate equation of state that is described in Appendix A. We initialize a uniform, isolated spherical core with total mass  $M_c = 1.0 M_\odot$ , and radius  $R_c = 10^{17} \text{ cm} \approx 6684 \text{ AU}$ . This corresponds to an initial mass density  $\rho_0 = 4.77 \times 10^{-19} \text{ g cm}^{-3}$  and a number density for molecular hydrogen  $n(\text{H}_2) = 1.2 \times 10^5 \text{ cm}^{-3}$  (assuming mean molecular weight  $\mu = 2.36$ ). The free-fall time of the core is thus  $t_{\text{ff}} = 3 \times 10^{12} \text{ s} \approx 9.6 \times 10^4 \text{ yr}$ . The initial core is rotating as a solid-body with angular speed  $\omega_0 = 1 \times 10^{-13} \text{ s}^{-1}$  for slow rotating case, and  $2 \times 10^{-13} \text{ s}^{-1}$  for fast rotating case, corresponding to a ratio of rotational to gravitational energy  $\beta_{\text{rot}} \approx 0.025$  and  $0.1$  (Goodman et al. 1993), respectively. The initial core is threaded by a uniform magnetic field along the rotation axis with a constant strength  $B_0$  of  $4.25 \times 10^{-5} \text{ G}$  for strong field case and  $2.13 \times 10^{-5} \text{ G}$  for weak field case, which gives a dimensionless mass-to-flux ratio  $\lambda (\equiv \frac{M_c}{\pi R_c^2 B_0} 2\pi\sqrt{G})$  of 2.4 and 4.8, respectively. It is consistent with the mean value of  $\lambda$  inferred from the OH Zeeman observations by Troland & Crutcher (2008).

We adopt the spherical coordinate system  $(r, \theta, \phi)$  and non-uniform grid to provide high resolution towards the innermost region of simulation domain. The inner boundary has a radius  $r_{\text{in}} = 3 \times 10^{13} \text{ cm} = 2 \text{ AU}$  and the outer has  $r_{\text{out}} = 10^{17} \text{ cm}$ . At both boundaries, we impose a standard outflow boundary conditions to allow matter to leave the computational domain. The mass accreted across the inner boundary is collected at the centre as the stellar object. We use a total of  $120 \times 96 \times 96$  grid points. The grid is uniform in the  $\phi$ -direction, non-uniform in the  $\theta$ -direction with  $\delta\theta = 0.6713^\circ$  near the equator, and non-uniform in the  $r$ -direction with a spacing  $\delta r = 0.1 \text{ AU}$  next to the inner boundary. The  $r$ -direction spacing increases geometrically outward by a constant factor of  $\sim 1.0733$ , and the  $\theta$ -direction spacing increases geometrically from the equator to either pole by a constant factor of  $\sim 1.0387$ .

In most models of this study, we fix the cosmic-ray ionization rate at the cloud edge to be  $\zeta_0^{\text{H}_2} = 1.0 \times 10^{-17} \text{ s}^{-1}$ , with a characteristic attenuation length of  $96 \text{ g cm}^{-2}$ . We do not consider the high cosmic-ray ionization case of  $\zeta_0^{\text{H}_2} = 5.0 \times 10^{-17} \text{ s}^{-1}$  of Zhao+16, where disc formation is strongly suppressed unless both  $\beta_{\text{rot}}$  and  $\lambda$  are high. We choose two grain size distributions, MRN and tr-MRN for the computation of non-ideal MHD diffusivities. Both size distributions have the same power law index  $-3.5$  and maximum grain size  $a_{\text{max}} = 0.25 \text{ \mu m}$ , but different minimum grain sizes  $a_{\text{min}} = 0.005 \text{ \mu m}$  (MRN) and  $0.1 \text{ \mu m}$  (tr-MRN). As compared to Zhao+16, we dropped the large grain (LG) case, as we find its effect on disc formation is in between the MRN and tr-MRN cases. The simulation models are summarized in Table 1.

<sup>1</sup> Merely for convenience, we follow the axisymmetric prestellar collapse in 2D until well before the formation of a first hydrostatic core (Larson 1969), and restart the simulation in full 3D thereafter.

<sup>2</sup> The momentum transfer rate coefficients are parametrized as a function of temperature according to Table 1 of Pinto & Galli (2008).

**Table 1.** Model Parameters & Result Summary

Model	Grain Size	$\lambda$	$\beta_{\text{rot}}$	Morphology	Initial Disc/Ring Radius (AU)	Spiral Structure Radius (AU)	Circumstellar Disc Average Radius (AU)
2.4Slw-MRN	MRN	2.4	0.025	DEMS	–	–	–
2.4Slw-trMRN	tr-MRN	2.4	0.025	Disc+Spiral	~15	~40	~20
2.4Fst-MRN	MRN	2.4	0.1	DEMS	–	–	–
2.4Fst-trMRN	tr-MRN	2.4	0.1	Ring→Disc+Spiral	~30	~100 $\uparrow$	~15
4.8Slw-MRN	MRN	4.8	0.025	DEMS+Disc <sup>Trans</sup>	~15	–	–
4.8Slw-trMRN	tr-MRN	4.8	0.025	Ring→Disc+Spiral <sup>Frag</sup>	~25	~150 $\uparrow$	~20
4.8Fst-MRN	MRN	4.8	0.1	Disc <sup>Shrink</sup> →DEMS	~20	–	~10→0
4.8Fst-trMRN	tr-MRN	4.8	0.1	Ring <sup>Frag</sup>	~40	~200 $\uparrow$	~10
HydroSlw	–	$\infty$	0.025	Ring <sup>Frag</sup> →Multiples	~50–100	~500 $\uparrow$	~20
HydroFst	–	$\infty$	0.1	Ring <sup>Frag</sup> →Multiples	~70–150	~1000 $\uparrow$	~20

† MRN: full MRN distribution with  $a_{\text{min}} = 0.005 \mu\text{m}$ ,  $a_{\text{max}} = 0.25 \mu\text{m}$

† tr-MRN: truncated MRN with  $a_{\text{min}} = 0.1 \mu\text{m}$ ,  $a_{\text{max}} = 0.25 \mu\text{m}$

† DEMS: Decoupling-Enabled Magnetic Structures (Zhao et al. 2011).

† RSD<sup>Trans</sup>: a transient RSD appears early on due to the high angular momentum initially, but disappears within  $10^3$  yr.

† RSD<sup>Shrink</sup>: initially forms a RSD but shrinks in size over time ( $\sim 10^3$  yr).

† Spiral<sup>Frag</sup> or Ring<sup>Frag</sup>: fragmentation occurs in spirals or rings, leading to the formation of binary and multiple systems.

†  $\uparrow$ : the radius of the spiral structure (or centrifugal radius) continues to increase over time.

### 3 SIMULATION RESULTS

As shown in Table 1, the conditions for disc formation are largely similar to Zhao+2016, with formation of rotational supported structures occurring in all tr-MRN cases, compared to no disc, transient disc, or shrinking disc in the MRN cases. The main difference from Zhao+16 is the variety of disc morphologies shown in 3D, ranging from DEMS (Decoupling-Enabled Magnetic Structures; Zhao et al. 2011) to RSDs, and from spiral to ring structures. In cases with lower magnetization ( $\lambda = 4.8$ ), fragmentation often occurs within spirals and rings that leads to the initial formation of binary and multiple systems.

#### 3.1 AD-Enabled Disc Formation: Field Decoupling in the Envelope

Despite existing literature on field decoupling in the high density disc itself, we find the key for disc formation lies in the field decoupling in the protostellar envelope. Particularly, an enhanced AD in the absence of VSGs (Zhao+16) ensures sufficient magnetic flux to be decoupled in the low-density envelope before reaching the inner tens-of-AU stellar vicinity, thus preventing the “catastrophic” magnetic braking and preserving sufficient angular momentum for disc assembly.

##### 3.1.a Truncated tr-MRN Model: 2.4Slw-trMRN

Fig. 1 shows the face-on view of the equatorial disc-spiral structure in the 2.4Slw-trMRN model at 131.096 kyr, about 4.56 kyr after the formation of first core. The velocity profile clearly shows that the inner ~20 AU disc is rotating with Keplerian speed. The spiral structure is likely infall streams onto the Keplerian disc. The effective centrifugal pressure  $P_{\text{cent}} = \frac{1}{2}\rho v_{\phi}^2$  in the disc is ~10 times higher than the thermal pressure, indicating that the disc is primarily rotationally supported (see Fig. 2). The plasma- $\beta$  ( $\equiv \frac{P_{\text{th}}}{P_{\text{B}}}$ , where  $P_{\text{th}}$  is the thermal pressure and  $P_{\text{B}}$  the magnetic pressure) in the disc is on the order of  $\sim 10^2$ . The disc rotation also wraps up mag-

netic field lines over time, producing the well-developed toroidal magnetic field components shown in the top-right panel of Fig. 1.

The direct evidence of magnetic decoupling in the envelope is the significant separation between the infall velocity of neutral gas  $v_r$  and that of the ions  $v_{\text{I}}$  (bottom-right panel of Fig. 1). The ion velocity is in fact an “effective ion velocity” defined as  $\mathbf{v}_{\text{I}} \equiv \mathbf{v} + \mathbf{v}_{\text{d}}$ , where  $\mathbf{v}_{\text{d}}$  is the drift velocity of the magnetic field given in Eq. 1. Because AD in zeusTW is treated using an explicit method (Mac Low et al. 1995; Li et al. 2011) and  $\mathbf{v}_{\text{I}}$  is directly used to evolve the magnetic field, hence  $\mathbf{v}_{\text{I}}$  actually denotes the velocity of the magnetic field.<sup>3</sup> The nearly zero effective ion velocity<sup>4</sup>  $v_{\text{I}}$  at ~50 AU–300 AU implies that magnetic fields have almost decoupled from the bulk infall motion of neutral gas and are left behind in the envelope. Such an efficient decoupling is a result of the enhanced AD at low density regimes ( $\lesssim 10^{10} \text{ cm}^{-2}$ ) in the absence of VSGs (Zhao+16; see their Section 4 and Fig. 2). It is clearly manifested in the bottom-left panel of Fig. 1 that the AD diffusivity on the ~500 AU scale is already well-above  $10^{18} \text{ cm}^2 \text{ s}^{-1}$ , which is at least one order of magnitude higher than the infalling region in the 2.4Slw-MRN model (shown next).

##### 3.1.b MRN Grain Model: 2.4Slw-MRN

In the 2.4Slw-MRN model, the physical structure of the central region is drastically different. No obvious RSD forms at all (Fig. 3); instead, large torus-shaped DEMS occupy the inner ~150 AU, which consist essentially of the decoupled flux from the accreted matter

<sup>3</sup> In reality, different charged species are attached to the magnetic field to different degrees, and the velocity of individual charged species can differ from the magnetic field velocity. We refer the readers to Kunz & Mouschovias (2009, 2010) for detailed discussions.

<sup>4</sup> The velocity profile is plotted along a line cut within  $0.336^\circ$  of the equator; however, the infall stream in this model does not lie on the equator and lands upon the disc from the upper hemisphere (see § 3.1.c and Fig. 5). Therefore, the actual decoupling region along the infall stream should be slightly bigger and a moderate decoupling indeed occurs near 20 AU as well.

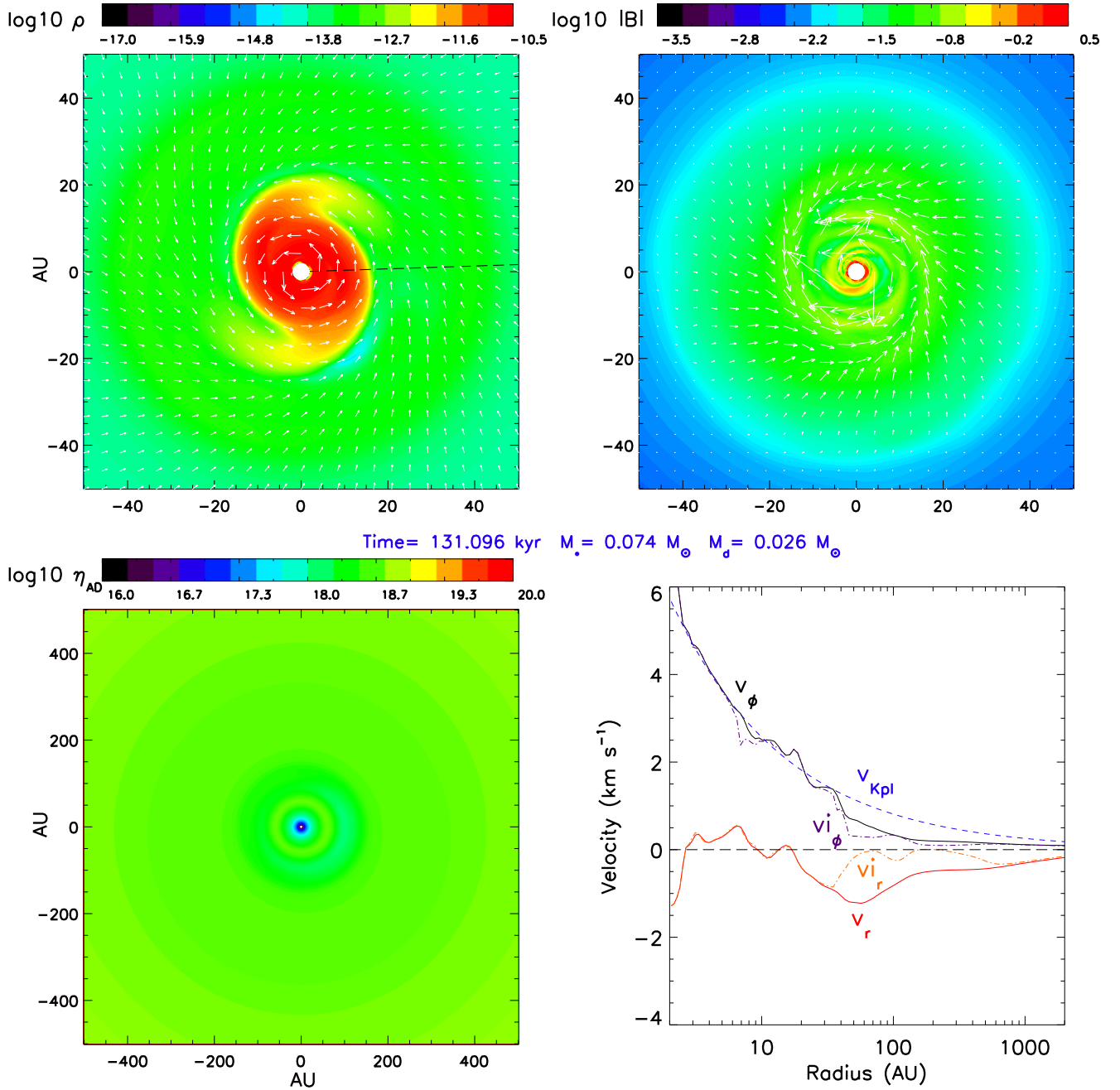


**Figure 1.** Distributions of logarithmic mass density  $\rho$  ( $\text{g cm}^{-3}$ ), magnetic field strength  $|B|$  (G), and ambipolar diffusivity  $\eta_{AD}$  ( $\text{cm}^2 \text{s}^{-1}$ ) within  $0.336^\circ$  of the equator, and velocity profile along the  $\phi = 1.9^\circ$  line cut (black dashed line in the top-left panel) for the 2.4Slw-trMRN model at time  $t \approx 131.1 \text{ kyr} = 1.36 t_{\text{ff}}$ . The projected velocity field (top-left) and magnetic field (top-right) are shown as white arrows. Length unit of the axes is in AU. The typical temperature in the disc is around 100 K.

(Zhao et al. 2011; Krasnopolsky et al. 2012). Accordingly, the magnetic field strength is also higher in the low density DEMS. Such a structure expands over time from a few AU to a few 100 AU, which blocks infall and obstructs rotation over a large region on the equator. Gas finds other paths to reach the centre, however, dragging in most magnetic field lines as well (bottom right panel of Fig. 3, plotted along a line cut in the positive x-direction). Unlike the 2.4Slw-trMRN model, the effective ion velocity is almost indistinguishable from the bulk neutral velocity beyond 70 AU; There is

only a partial separation between  $v_{i,r}$  and  $v_r$  in the inner  $\sim 20\text{--}70$  AU; yet the separation is not as large as in the 2.4Slw-trMRN model. As most of the magnetic field is dragged all the way to the centre and eventually decouples at the inner boundary ( $\sim 2$  AU) from the

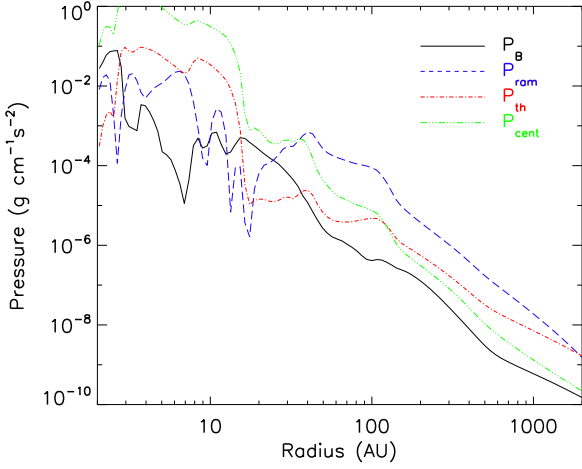


**Figure 2.** Profile of thermal  $P_{\text{th}}$ , magnetic  $P_B$ , ram  $P_{\text{ram}}$ , and effective centrifugal  $P_{\text{cent}}$  pressures within  $0.336^\circ$  of the equator, along the same line cut as the velocity profile in Fig. 1.

accreted matter that enters the sink hole<sup>5</sup> it joins the existing DEMS or creates new DEMS in directions of least resistance.

As shown in Fig. 4, the infall velocity for the northern DEMS component shows clear expansion with  $v_r$  and  $v_i$  being positive between  $\sim 50$ – $200$  AU. Very little rotation is present across the DEMS. The equatorial region within  $\sim 30$ – $200$  AU is dominated by magnetic pressure  $P_B$ ; and the innermost  $\sim 30$  AU is dominated by both magnetic and ram pressures, which implies magnetic instability of the interchange type (rising of more strongly magnetized material against less strongly magnetized collapsing flow, e.g., Parker 1979)

In comparison to the 2.4Slw-trMRN model above, the primary reason for the failure of disc formation and the presence of DEMS is that too much magnetic flux has been brought to the centre. It is a direct consequence of the low ambipolar diffusivity in the infalling envelope beyond  $\sim 10^2$  AU (number density  $\sim 10^7$  g cm<sup>-3</sup>– $10^{10}$  g cm<sup>-3</sup>). Apart from the expanding DEMS, the  $\eta_{\text{AD}}$  is mostly around  $10^{17}$  cm<sup>2</sup> s<sup>-1</sup> within the 500 AU region (bottom left panel of Fig. 3) — at least one order of magnitude lower than the values in the 2.4Slw-trMRN model. This leads to very little decoupling of magnetic field from the infall flow, and hence an excessive amount of magnetic flux reaching the centre. Although a certain degree of field decoupling indeed occurs in the inner few tens of AU, it does not prevent enough magnetic flux from accumulating in the central region and hence is unable to save the disc. The drastic difference between the two models, is simply caused by changing a single parameter – the grain size distribution.

### 3.1.c Collapse Induced Pinching of B-Fields & B-Field Decoupling in the Envelope

In the tr-MRN cases where VSGs are absent, the regions of field decoupling expand over time from a few tens of AU to a few  $10^3$  AU into the envelope. As shown in Fig. 5, the effective infall velocity of

<sup>5</sup> When magnetic field lines are dragged to the inner boundary, they are free to move around after detaching from the accreted matter. Therefore, the total magnetic flux is conserved (unlike Wurster et al. 2017).

ions  $v_i$  is close to 0 between 30–80 AU at an early time  $t \approx 127.4$  kyr ( $\sim 850$  yr after the formation of the first core), along with a well-decoupled zone between 20–100 AU. At  $t \approx 132.1$  kyr, regions of zero  $v_i$  are located between 40–400 AU, and the decoupling region extends further to 20–600 AU. At the later time  $t \approx 146.0$  kyr,  $v_i$  has reached 0 in a wide equatorial region between 70–2000 AU, and is mostly separated from the neutral infall velocity  $v_r$  between 20–2000 AU. Note that the effective rotational velocity of ions  $v_{i\phi}$  is mostly identical to the neutral  $v_\phi$ , with a moderate separation in the inner  $\sim 100$  AU, where poloidal magnetic fields start to wind up to generate the toroidal field components and a corresponding radial currents across the “pseudo-disc” (Galli & Shu 1993).

The large separation between  $v_i$  and  $v_r$  in the tr-MRN case indicates a notable radial drift of magnetic field relative to the neutrals, i.e., field decoupling from the collapsing flow. We show below that the location of the decoupling region is tied closely to the regions with strong pinching of magnetic field by the collapsing flow. Therefore, the expansion of the decoupling region is a natural consequence of the inside-out collapse that gradually induces the field pinching at larger and larger radii along the equator.

The drift velocity  $\mathbf{v}_d$  of the magnetic field relative to the neutrals due to AD is defined as,

$$\mathbf{v}_d = \frac{\eta_{\text{AD}}}{\mathbf{B}^2} (\nabla \times \mathbf{B}) \times \mathbf{B}. \quad (1)$$

In a spherical coordinate system, the  $r$ -direction component of the drift velocity can be written as,

$$\begin{aligned} v_{d,r} &= \frac{\eta_{\text{AD}}}{\mathbf{B}^2} [(\nabla \times \mathbf{B})_\theta B_\phi - (\nabla \times \mathbf{B})_\phi B_\theta] \\ &\approx -\frac{\eta_{\text{AD}}}{\mathbf{B}^2} \frac{B_\theta}{r} \left[ \frac{\partial}{\partial r}(rB_\theta) - \frac{\partial B_r}{\partial \theta} \right], \end{aligned} \quad (2)$$

where we ignore the contribution of  $(\nabla \times \mathbf{B})_\theta B_\phi$  because in the collapsing envelope both the magnetic current in the  $\theta$ -direction and the field strength in the  $\phi$ -direction (toroidal field) are much smaller than the other corresponding components.

Along the equator,  $B_\theta$  is essentially the vertical poloidal field; however, the gradient of such fields along the radial direction is much smaller compared to the change of  $B_r$  across the  $\theta = 90^\circ$  equatorial plane, where the sign of  $B_r$  is reversed at the pinching point. Therefore, the  $r$ -directional drift velocity can be further simplified to,

$$v_{d,r} \approx \frac{\eta_{\text{AD}}}{\mathbf{B}^2} \frac{B_\theta}{r} \frac{\partial B_r}{\partial \theta}, \quad (3)$$

which depends mainly on the ambipolar coefficient  $\eta_{\text{AD}}/\mathbf{B}^2$  and the tension term of the Lorentz force  $(B_\theta/r)(\partial B_r/\partial \theta)$ . Fig. 6 shows that the ambipolar coefficient at different times in the tr-MRN case does not change much over a wide region ( $\gtrsim 30$  AU) outside the disc, which cannot be responsible for the expansion of the decoupling region over time. However, their values in the envelope are indeed a factor of 10 or more larger than in the MRN case, which explains the absence of fully decoupled regions in the MRN case shown in Fig. 3.

After eliminating the role of  $\eta_{\text{AD}}/\mathbf{B}^2$ , we are left with only one possibility to account for the expansion of the decoupling region — the tension force  $(B_\theta/r)(\partial B_r/\partial \theta)$ . In Fig. 7, we plot the different terms of the Lorentz force based on Eq. 2–3, along a line through the curved infall stream (or pseudo-disc, see sketch in the bottom panel of Fig. 5) that properly captures the positions with the most severe pinching of magnetic field lines. When comparing curves of different times, the tension term  $(B_\theta/r)(\partial B_r/\partial \theta)$  clearly shows larger values in the corresponding decoupling regions. For instance,

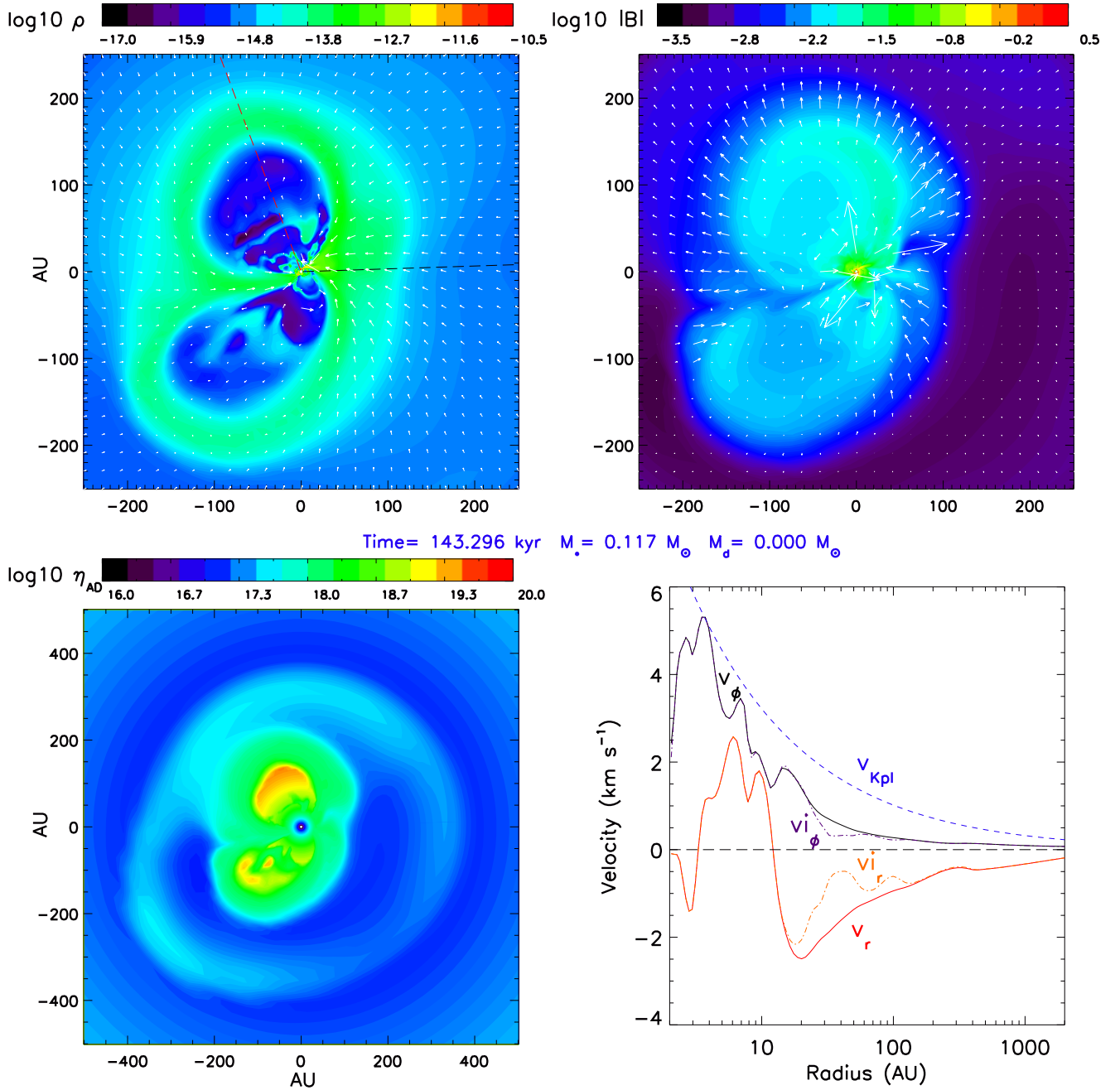


**Figure 3.** Distributions of logarithmic mass density  $\rho$  ( $\text{g cm}^{-3}$ ), magnetic field strength  $|B|$  (G), and ambipolar diffusivity  $\eta_{AD}$  ( $\text{cm}^2 \text{s}^{-1}$ ) within  $0.336^\circ$  of the equator, and velocity profile along the  $\phi = 1.9^\circ$  line cut (black dashed line in the top-left panel) for the 2.4SIw-MRN model at time  $t \approx 143.3 \text{ kyr} = 1.49 t_{ff}$ . The projected velocity field (top-left) and magnetic field (top-right) are shown as white arrows. Length unit of the axes is in AU. The red dashed line in the top-left panel is the line cut used in Fig. 4.

at  $t \approx 1.372 t_{ff}$ , the tension term between 100–600 AU is about 10 times higher than that at an early time  $t \approx 1.322 t_{ff}$  that has a decoupling region between 20–100 AU. Hence, the total decoupling zone at  $t \approx 1.372 t_{ff}$  is combined into 20–600 AU, which matches the velocity separation in Fig. 5. A similar reasoning applies to  $t \approx 1.516 t_{ff}$  that yields an even wider decoupling zone between 20–2000 AU; this again matches the above-mentioned velocity separation.

Note that the three terms  $(B_\theta/r)(\partial B_r/\partial\theta)$ ,  $(-\nabla \times \mathbf{B})_\phi B_\theta$ , and

$[(\nabla \times \mathbf{B}) \times \mathbf{B}]_r$  are almost identical to each other, with only very small discrepancies in the inner 20 AU. This validates the approximations we made in Eq. 2–3. Indeed, the gradient of  $B_\theta$  and the whole term  $(\nabla \times \mathbf{B})_\phi B_\theta$  are more chaotic and orders of magnitude smaller than their respective counterparts. The dominance of tension force among the Lorenz force terms and its expansion in radius over time therefore proves the collapse triggered field pinching to be the main reason for the large expanding decoupling region in the envelope.

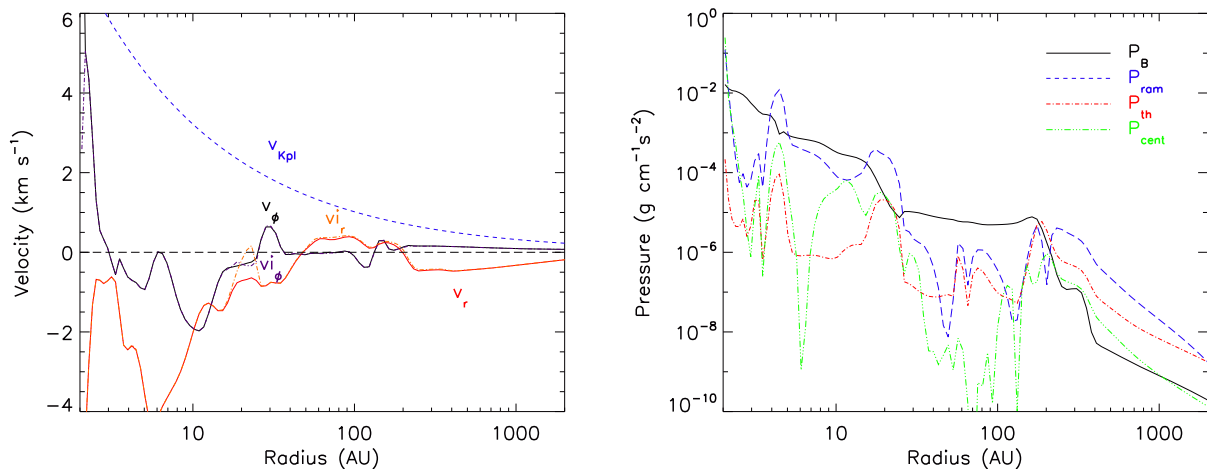


**Figure 4.** Left panel: profile of equatorial infall and rotation speed in the 2.4Slw-MRN model at  $t \approx 143.3$  kyr (same time as in Fig. 3). The Keplerian speed is plotted based on the central mass. Right panel: profile of equatorial thermal  $P_{\text{th}}$ , magnetic  $P_{\text{B}}$ , ram  $P_{\text{ram}}$ , and effective centrifugal  $P_{\text{cent}}$  pressures. Both panels are plotted along a line cut through the DEMS with  $\phi = 111^\circ$  (red dashed line in the top-left panel of Fig. 3).

The mechanism of this type of field decoupling is summarized in the illustration Fig. 8.

As collapse proceeds, the efficient field decoupling prevents a large fraction of the magnetic flux from moving inward with the collapsing neutral flow. We thus expect the mass-to-flux ratio  $\lambda$  to increase over time, which is exactly the case in Fig. 9.  $\lambda$  increases from 2–3 at the cloud edge to  $\sim 10$ ,  $\sim 100$ , and  $\sim 200$  near the centre at time  $1.322t_{\text{ff}}$ ,  $1.372t_{\text{ff}}$ , and  $1.516t_{\text{ff}}$ , respectively. In comparison,  $\lambda$  in the MRN model at time  $1.487t_{\text{ff}}$  kyr is a few times lower than that of the tr-MRN cases outside  $\sim 100$  AU. For regions inside  $\sim 100$  AU, we compare the MRN case with the tr-MRN case at time  $1.372t_{\text{ff}}$ , in that they are similar in terms of total star plus disc mass.

The mass-to-flux ratio  $\lambda$  in the tr-MRN model at  $1.372t_{\text{ff}}$  is no less than the MRN model at  $1.487t_{\text{ff}}$ . It is indeed caused by a difference in magnetic flux (inside a given cylinder) shown in Fig. 10, since the two cases are comparable in mass evolution. Inside  $\sim 2000$  AU, the specific angular momentum is already a factor of a few higher in the tr-MRN case than in the MRN case, which is consistent with the result in Zhao+16. Such a difference is even larger in the inner  $\sim 200$  AU where DEMS reside. Note that the infalling gas piles up at  $\sim 200$ – $300$  AU outside the DEMS in the MRN case, hence resulting in a small plateau in the specific angular momentum outside the DEMS. Therefore, the excessive magnetic flux in the MRN model both lowers the specific angular momentum of the infalling gas in a wide region, and results in the magnetically dominated DEMS that obstruct the rotation in the innermost disc forming region.

To conclude, it is worth noting that the decoupling region occurs preferentially in the vicinity of the infall channel where field pinching is the strongest (similar to Krasnopolsky & Königl 2002). In an axisymmetric collapse, such a channel is along the equator. Larger than  $\sim 3^\circ$  (with respect to the origin) above or below the equator, the separation of infall velocity between the magnetic field and the neutrals nearly disappears in either the MRN or tr-MRN models. Besides, the AD decoupling of magnetic fields triggered by collapse requires a lack of VSGs before the onset of discs, in order to provide enough ambipolar diffusivity in the envelope. Therefore, the process of removing VSGs must have already taken place in the  $10^3$  AU scale envelope or even in the prestellar phase.

### 3.2 Trapping and Escaping of Early DEMS in Discs

As shown in Zhao et al. (2011) and Krasnopolsky et al. (2012) for both the ideal MHD limit and non-ideal MHD cases, DEMS are inevitable structures once magnetic flux is by any means decoupled from the accreted matter (onto the star). In § 3.1.b, we have demonstrated the catastrophic role of DEMS in suppressing disc formation and obstructing disc rotation in the MRN cases. However, in the tr-MRN models, the DEMS are still present, but are less destructive and play a less important role.

In the tr-MRN models, the DEMS are most prominent in early phases shortly after the first core formation, as gas in the cloud centre that has the lowest specific angular momentum is quickly accreted by the star. As shown in Fig. 11, the corresponding decoupled magnetic flux remains in the stellar vicinity, and is surrounded by the early RSD formed from the infalling gas with higher specific angular momentum (2nd–5th panels from the left).

At the beginning, the axisymmetric first core (1st panel from the left) breaks into filamentary accretion flows (2nd panel from the left) in between DEMS under the so-called magnetic interchange instability (Parker 1979; Kaisig et al. 1992; Stehle & Spruit 2001; Krasnopolsky et al. 2012). The DEMS (high magnetic field strength and low density regions dominated by  $P_{\text{B}}$ ) tend to expand as the central star grows in mass and more magnetic flux is decoupled (3rd panel from the left); however, the structures are quickly contained and squeezed by the  $\sim 10$  AU initial ring-shaped RSD (4th panel from the left). The RSD (high density disc regions dominated by  $P_{\text{cent}}$ ), which is unrelated to the already disrupted first core, is formed by assembling infalling gas with large enough centrifugal radius, thanks to the efficient decoupling of magnetic flux at larger radii that allows gas to retain enough angular momentum along their way to the centre (as discussed above in § 3.1.c). Within a few 100 yr, the RSD quickly grows and becomes massive enough ( $\gtrsim 50\%$  of stellar mass) to be self-gravitating (Toomre  $Q$  parameter  $\sim 0.2$ , see Fig. 15) and develops spiral structures that open up escape channels for DEMS (6th panel from the left).

At later times, the DEMS are less obvious and become even less disruptive to disc evolution, as most magnetic flux is excluded from

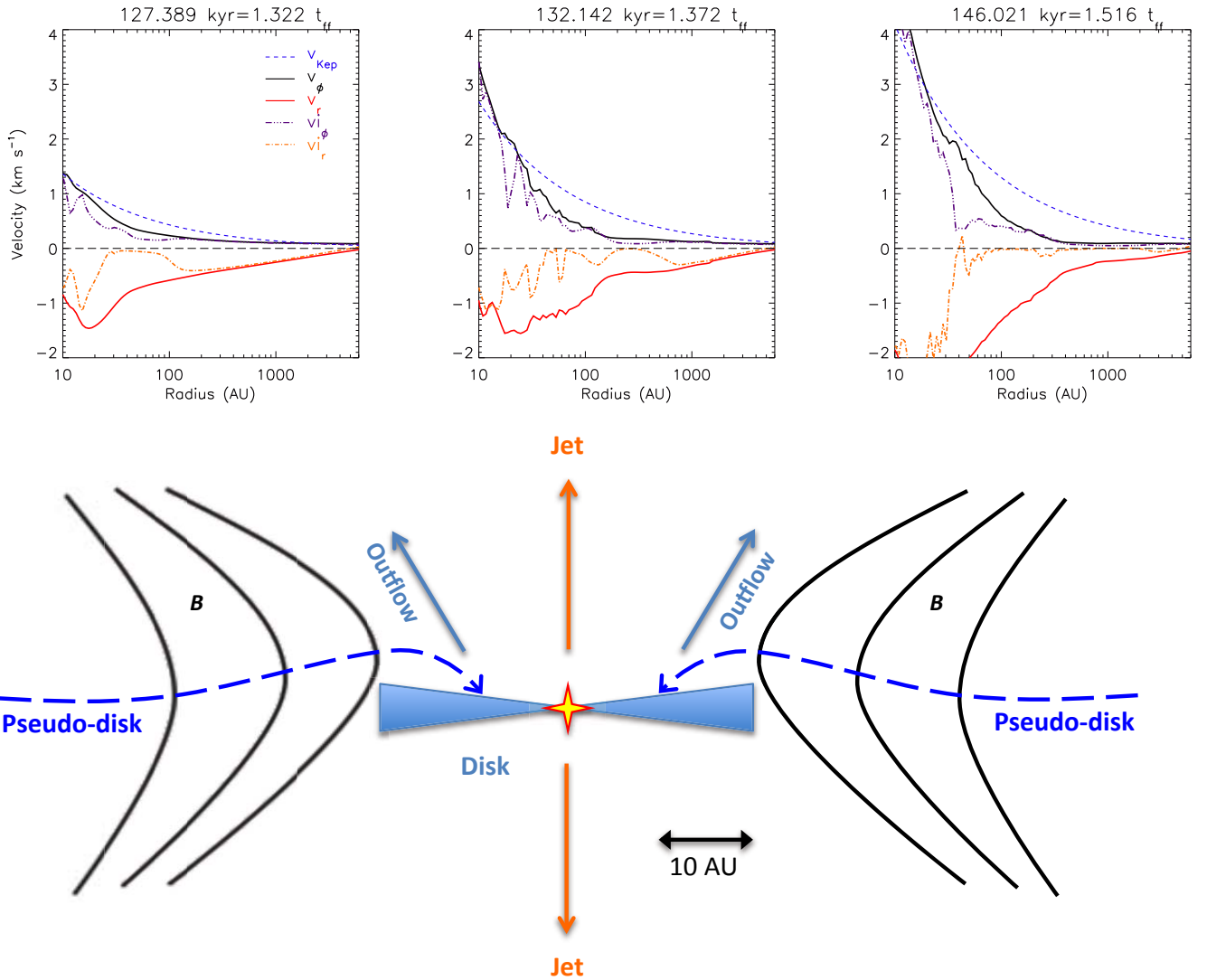


**Figure 5.** Top row: velocity profiles for the 2.4Slw-trMRN model at time  $t=1.322 t_{\text{ff}}$ ,  $1.372 t_{\text{ff}}$ , and  $1.516 t_{\text{ff}}$ , along the curved infall stream or the pseudo-disk where field pinching are the strongest. Bottom row: illustration of the equatorial RSD and the curved pseudo-disk for the 2.4Slw-trMRN model (see also Fig. 19). Such a configuration is persistent rather than transient.

the thermally- and rotationally-dominated disc.<sup>6</sup> In other words, a sizeable RSD ( $\geq 10$  AU) further prevents magnetic flux from reaching the very centre and minimizes the development of DEMS around the star. Recall that to form and retain such a RSD requires enough angular momentum in the infalling gas, which is achieved in the trMRN models. We will show a shrinking disc example in the MRN model in § 3.4 where the initial RSD can quickly shrink into the central sink hole by accreting gas with low specific angular momentum; in such a case, large DEMS re-appear at later times.

It is worth clarifying that the development of DEMS is a natural result of magnetic flux conservation and does not depend on the de-

tailed decoupling mechanisms (Ohmic, AD, or Hall; see Krasnopolsky et al. 2012). The results in this section also imply that

- (i) the first hydrostatic core (Larson 1969) is prone to disruption by magnetic instabilities and is unlikely the origin of the RSD formed later, in contrast to the claims by previous studies (Bate 1998, 2010, 2011; Machida & Matsumoto 2011);
- (ii) the onset of RSD takes place outside the DEMS region, which is enabled by the sufficient angular momentum in the infalling gas;
- (iii) after a sizeable RSD ( $\geq 10\text{--}15$  AU) is in place, most magnetic flux can be further kept outside the disc, or the centrifugal radius of the infalling gas (definition given in Eq. 6) if it is smaller than the disk radius.

### 3.3 Disc Fragmentation & Formation of Multiple Systems

Until recently, disc fragmentation has shown to be difficult if the initial core is moderately or strongly magnetized ( $\lambda \lesssim 10$ ) (e.g., Lewis & Bate 2017). In contrast, we find that fragmentation can

<sup>6</sup> Note that the RSD and the pseudo-disk in the 2.4Slw-trMRN model are non-coplanar (Fig. 5, see also Li et al. 2014). Despite the unusual geometry, the infall stream along the pseudo-disk still lands relatively far from the central star, with a radial distance between 10–15 AU (centrifugal radius, see also § 3.4 for detailed discussions).



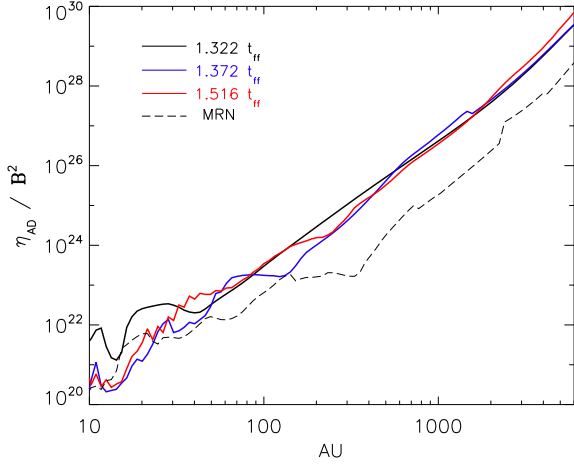


**Figure 6.**  $\eta_{AD}/B^2$  for three different times of the 2.4Slw-trMRN model, along with the 2.4Slw-MRN model at  $1.487t_{fr}$ . The values are plotted along the curved infall stream or the pseudo-disc.

indeed occur on spirals or rings in the tr-MRN models (Table 1) with a relatively strong initial magnetic field ( $\lambda = 4.8$ ). Note that the spiral or ring structures themselves are clear signs of high specific angular momentum entering the inner disc-forming region.

The general criterion for disc stability and spiral formation can be estimated by Toomre’s  $Q$  parameter (Toomre 1964),

$$Q = \frac{c_s \kappa}{\pi G \Sigma}, \quad (4)$$

where  $c_s$  is the sound speed within the disc,  $\kappa$  is the epicyclic frequency which equals to  $\Omega$  (angular rotation frequency) for a Keplerian disc, and  $\Sigma$  is the disc surface density. When  $Q \lesssim 1$ , the disc becomes susceptible to the growth of spiral wave modes, which is exactly the case in the early phases of all tr-MRN models. By substituting  $\Omega^2 \approx GM_*/r^3$ , disc mass  $M_d \approx \pi r^2 \Sigma$ , and disc scale height  $H \approx c_s/\Omega$ , Eq. 4 can be further simplified to the following approximation,

$$Q \approx 2 \frac{M_* H}{M_d R_d} \quad (5)$$

(Tobin et al. 2016), where  $M_*$  is the stellar mass and  $R_d$  the disc radius. To identify the disc in our simulations, we use the following criteria (similar to Joos et al. 2012):

- (i) Density is above certain critical value  $\rho_{cr}$ , i.e.,  $\rho > \rho_{cr} = 10^{-13} \text{ g cm}^{-3}$ ;
- (ii) Azimuthal velocity dominates over radial velocity, i.e.,  $v_\phi > f_{thres} v_r$ ;
- (iii) Rotational support dominates over both thermal and magnetic support, i.e.,  $\rho v_\phi^2/2 > f_{thres} P_{th}$ , and  $\rho v_\phi^2/2 > f_{thres} P_{mag}$ .

We choose  $f_{thres} = 2$  in our analysis. Note that the criterion of low magnetic support is generally not important, because the high density regions satisfying criterion (i) generally have plasma- $\beta$  on the order of  $\sim 10^1$ – $10^4$  (e.g., Fig. 2).<sup>7</sup> For the same reason, the magnetic Toomre parameter (Kim & Ostriker 2001; Seifried et al.

<sup>7</sup> The high density part of the spiral structures generally have plasma- $\beta$  on the order of  $\sim 10^1$ , while the plasma- $\beta$  in the disc is at least a few  $10^2$ .

2013) is almost identical to the standard Toomre  $Q$  parameter under the above criteria.

We apply these analyses to both the non-fragmenting (2.4Fst-trMRN) and fragmenting (4.8Slw-trMRN & 4.8Fst-trMRN) models. We confirm that the criterion  $Q \lesssim 1$  alone is insufficient for the occurrence of fragmentation; the instability induced spiral structures also have to accrete materials from the envelope more rapidly than it could transport them inward (Kratter et al. 2010). In our simulation, we observe that the fragments usually form at the local centrifugal barrier (sections of the spiral or ring structures, shown below) where the infall material piles up.

### 3.3.a Spiral Structures and Centrifugal Barrier: Model 2.4Fst-trMRN

In the 2.4Fst-trMRN model (higher magnetization), no obvious fragmentation takes place throughout the simulation even though Toomre  $Q < 1$  (see detailed discussion in § 3.3.d); instead, a grand spiral structure steadily develops in the central 100 AU region. As shown in Fig. 12, the early evolution is very similar to the 2.4Slw-trMRN model (slower rotation) above. The  $\sim 5$  AU first core (1st panel from the left) is quickly disrupted within  $\sim 600$  yr and the inner  $\sim 10$  AU region is occupied by the DEMS. Surrounding the DEMS, a RSD is assembled and gradually grows as gas with high specific angular momentum falls in (2nd panel from the left). This stage lasts about  $\sim 1.2$  kyr until the RSD grows more massive than the central star and becomes gravitationally unstable. As shown in Fig. 15, the disc mass catches up and overtakes the stellar mass around  $t \sim 160$  kyr, and the  $Q$  parameter decreases rapidly from  $\sim 1.0$  to  $\sim 0.2$ . In the 3rd panel from the left, the RSD is compressed by the infall into a ring shape and starts to wobble. The northern and southern sections of the ring accumulates materials faster than other ring sections, which rapidly breaks the ring symmetry. Within 1/4 orbit, the two mass-gaining regions are turned into two spirals while the other ring sections fall to the centre. During the process, the DEMS find open channels to escape from the inner region, similar to the 2.4Slw-MRN case. Thereafter, accretion streams are able to wrap around the central star to form a well-defined disc. In another  $\sim 1000$  yr, the whole disc-spiral structure extends to  $\sim 100$  AU.

The development of these rotationally supported structures (disc, ring and spiral) is essentially controlled by the centrifugal radii (angular momentum) of infalling gas parcels. Approximately, the expected centrifugal radius  $R_{cent}(r)$  for gas in any given shell  $r$  can be expressed as,

$$R_{cent}(r) = \frac{j(r)^2}{G(M_* + \int_{r' < r} M(r'))}, \quad (6)$$

(Zhao+16), where  $M_*$  is the stellar mass and  $j(r)$  is the averaged specific angular momentum in that shell; however, when computing  $j(r)$ , we only consider materials within  $\pm 45^\circ$  above and below the equator ( $45^\circ < \theta < 135^\circ$ ) to avoid the bipolar outflow regions. The mass integration is still carried out using the total mass inside radius  $r$  for an approximated spherical potential.

The distribution of  $R_{cent}(r)$  is plotted in the second row of Fig. 12 for the corresponding snapshots in the top row. Except for the first core phase ( $M_* \lesssim 10^{-3} M_\odot$ ), the rest has a common “plateau” feature in the  $R_{cent}$  curve. It is a typical signature of the “so-called” centrifugal barrier (Zhao+16) because the infalling gas at different radii along the “plateau” tends to arrive at the same radius  $R_{cent}$ . Such centrifugal radii are around 20–30 AU (2nd panel from the left), 30–40 AU (3rd panel from the left), 40–50 AU (4th panel from

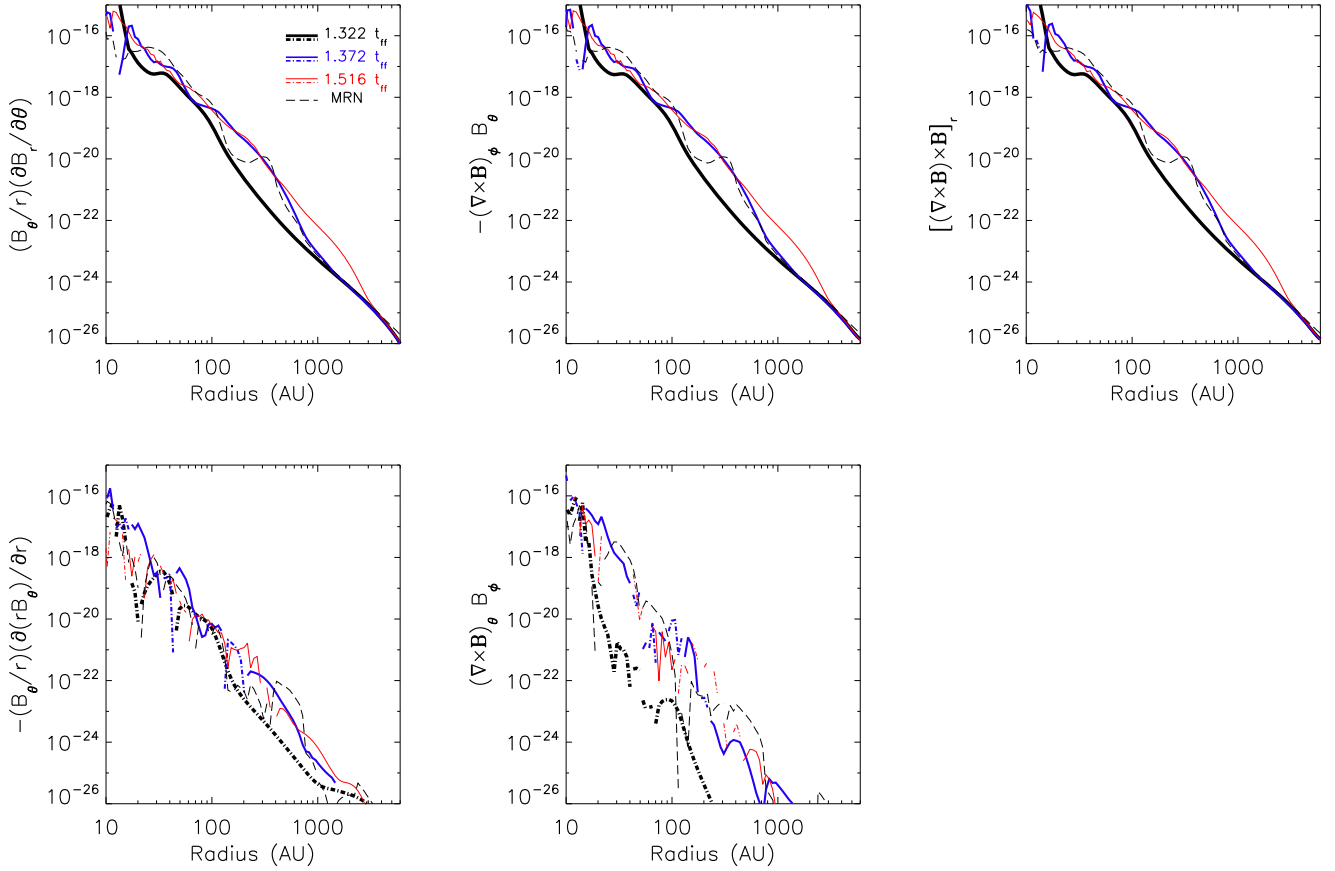


**Figure 7.** Lorentz force terms  $(B_\theta/r)(\partial B_r/\partial\theta)$ ,  $(-\nabla \times \mathbf{B})_\phi B_\theta$ ,  $[(\nabla \times \mathbf{B}) \times \mathbf{B}]_r$ ,  $(B_\theta/r)(\partial r B_\theta/\partial r)$ , and  $(\nabla \times \mathbf{B})_\theta B_\phi$  for the three different times of the 2.4Slw-trMRN model, along with the 2.4Slw-MRN model at  $1.487t_{ff}$ . Solid lines represent positive values and dot-dashed ones represent negative values. The values are plotted along the curved infall stream or the pseudo-disc.

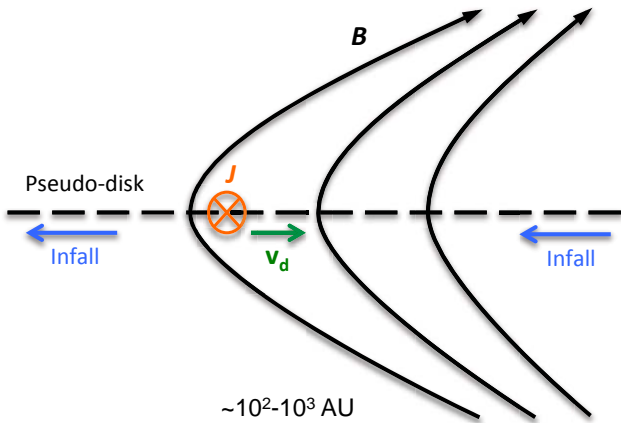


**Figure 8.** Illustration of AD drift in the collapsing envelope, in which  $\mathbf{J} = \frac{c}{4\pi} \nabla \times \mathbf{B}$  is the current induced by the field pinching across the pseudo-disc, and  $\mathbf{v}_d$  is the ambipolar drift velocity.

the left), and 70–80 AU (5th panel from the left) for the respective snapshots. As collapse continues to bring the envelope gas with

higher angular momentum (initial solid-body rotation), the location of the centrifugal barrier moves outward.

The centrifugal barrier can also be identified from the kinematic profiles. As the envelope gas falls towards the central region, its rotation speed  $v_\phi$  suddenly rises and infall speed  $v_r$  almost vanishes across the centrifugal barrier. Interior to the centrifugal barrier (post shock),  $v_\phi$  tends to decrease to the local Keplerian speed, unless the inner regions are dominated by the DEMS. It is worth pointing out that the centrifugal barrier at later times (4th and 5th panels from the left) coincides with the outer arm of the spiral structures, as compared to the rigid rings formed by piling up infall material shown in Zhao+16 (2D). In this sense, the centrifugal barrier in 3D is much less stiff or obstructive to the infall flows than in 2D.

### 3.3.b Fragmentation of Spirals & Accretion Bursts: Model 4.8Slw-trMRN

In the 4.8Slw-trMRN model with a low magnetization and slow rotation, fragmentation frequently occurs on the outer arm of the spiral structures, producing transient companion clumps with tens of Jupiter mass. In most cases, the companion clumps spiral inward and tidally interact with the circumstellar disc, leading to episodic accretion events (Fig. 16; see also Vorobyov & Basu 2006, 2015).

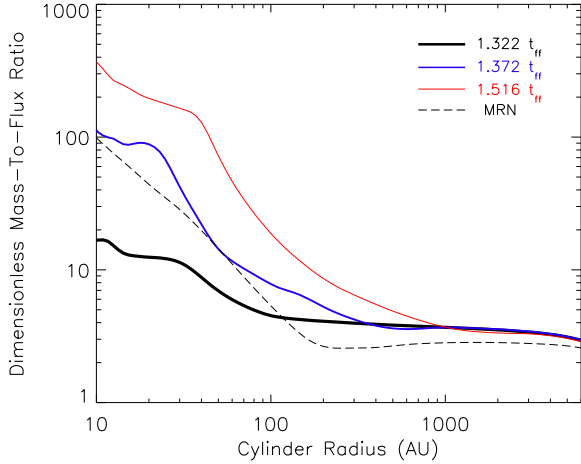


**Figure 9.** Dimensionless mass-to-flux ratio  $\lambda$ , for three different times of the 2.4Slw-trMRN model, along with the 2.4Slw-MRN model at  $1.487t_{\text{ff}}$ .

However, the orbital evolution of companion objects is not well followed in this study due to a lack of sink particle treatment (except for the stationary sink hole in the centre, which can violate the linear momentum conservation).

The early evolution of 4.8Slw-trMRN model is similar to that of the 2.4Slw-trMRN and 2.4Fst-trMRN models, in which the first core is disrupted by DEMS and an unstable RSD ( $Q \sim 0.3$  at 111.7–120.1 kyr, see Fig. 15) forms outside the DEMS from the infalling rotating materials. In Fig. 13, we present the phase when the spiral structure is already developed from the wobbling massive RSD (1st panel from the left,  $\sim 2.8$  kyr after the formation of the first core). A slight asymmetry causes the northern spiral arm to accumulate materials faster than the southern arm. Such a perturbation runs away rapidly within half orbital time, causing the northern arm to grow into a massive clump as it rotates to the southern position (2nd panel from the left). The massive clump, about 60% of the stellar mass of  $0.042 M_{\odot}$ , tidally disrupts the circumstellar disc. It is then followed by an accretion burst ( $\dot{M}_{*} \approx 6\text{--}7 \times 10^{-5} M_{\odot}/\text{yr}$ ) when materials flow along the stream from the clump onto the central star. Part of the clump wraps around the star to form a new circumstellar disc, and the rest continues to rotate and stretch into an arc shape. After another half orbit (3rd panel from the left), infalling materials pile up at the stretched northern arc at  $r \sim 70\text{--}80$  AU, i.e., the centrifugal barrier, where two companion objects form with a total mass of  $\sim 0.017 M_{\odot}$  ( $\sim 30\%$  of the stellar mass). The two companion clumps quickly merge into one clump with a mass of  $\sim 0.022 M_{\odot}$ , which spirals inward towards the star. After another 1/4 orbit (4th panel from the left), the circumstellar disc is disrupted again. The  $0.028 M_{\odot}$  clump near the  $0.068 M_{\odot}$  star causes another episode of accretion burst ( $\dot{M}_{*} \approx 6\text{--}7 \times 10^{-5} M_{\odot}/\text{yr}$ ). The situation afterwards is very similar to that of the first burst, where part of the clump wraps into a new circumstellar disc and the rest stretches out into long arc-shaped streams. Another 3/4 orbit later, a new clump of  $\sim 0.011 M_{\odot}$  ( $\sim 15\%$  of the stellar mass) forms near the  $\sim 100$  AU centrifugal barrier.

The subsequent evolution repeats the previous episodes in a similar fashion; and after two more accretion burst episodes, the system evolves into a more standard disc plus spiral configuration which extends to  $\sim 150$  AU. However, the outer spiral arm located

near the centrifugal barrier is still susceptible to the formation of  $10^{-2} M_{\odot}$  companion clumps.

It is worth verifying the location of the centrifugal barrier from both the centrifugal radius and the velocity profile (plotted along a line passing through the clumps). Basically the locations of the “plateau” on the  $R_{\text{cent}}$  curve and the sharp change in  $v_{\phi}$  and  $v_r$  coincide well with each other; and the location of such a centrifugal barrier also coincides with that of the companion clumps in the top panels. This indicates that the companion clumps are indeed formed from piling up infall material at the centrifugal barrier. Note that the curves of centrifugal radius inner to the centrifugal barrier are heavily affected by the companion objects at later times.

### 3.3.c Fragmentation of Rings & Multiple Systems: Model 4.8Fst-trMRN

In the faster rotating model 4.8Fst-trMRN, fragmentation of rings (formed due to high angular momentum influx) frequently produces multiple companion clumps. The early evolution of model 4.8Fst-trMRN however, has much smaller DEMS than the other cases, due to a lack of accretion onto the central star. Until  $t = 138.828$  kyr (2nd panel from the left of Fig. 14,  $\sim 2.2$  kyr after the formation of the first core), the stellar accretion rate is only around  $4 \times 10^{-7} M_{\odot}/\text{yr}$ . It is caused by the large angular momentum in the innermost  $\sim 5$  AU that prevents the gas from falling further below their large centrifugal orbits. Nevertheless, small DEMS can still develop in the inner 5 AU (1st panel from the left), which have disrupted the first core (similar to §. 3.2). Surrounding the DEMS is a  $\sim 10\text{--}15$  AU RSD with  $\sim 0.006 M_{\odot}$  formed from the gas with high specific angular momentum; Further out between 25–35 AU, a massive ring ( $0.024 M_{\odot}$ ) is growing outside the RSD by assembling gas from larger radii with even higher specific angular momentum. The ring has 4 times the mass of the inner RSD and 3 times the mass of the star, thus creating a gap between 15–25 AU by gradually attracting materials in the gap onto it (1st panel from the left). The massive ring quickly becomes gravitationally unstable, and wobbles and deforms within a few hundred years (about one orbital time). Tidal streams then develop, which connect the ring to the inner RSD (2nd panel from the left).

The eastern and western sections of the ring preferentially accrete the infall matter. After another 1/2 orbit, the original western ring section stretches into an arm around the inner disc, while the original eastern section forms a  $0.016 M_{\odot}$  companion clump that equals the stellar mass (3rd panel from the left). Gas near the clump also tends to orbit around it. However, the companion clump fails to survive the close approach 1/2 orbit later; it is tidally disrupted by the central star and produces an accretion burst with  $\dot{M}_{*} \sim 3 \times 10^{-5} M_{\odot}/\text{yr}$ . Note that the original 40 AU ring structure keeps expanding to 100–200 AU scales concurrently. About 500 yr after the accretion burst (4th panel from the left), two well-separated companion clumps develop within the ring structure, with mass  $\sim 0.008 M_{\odot}$  (northern) and  $0.010 M_{\odot}$  (southern), respectively. They sum up to 2/3 of the stellar mass. Subsequently, the triple system undergoes dynamic interactions, with the northern lighter companion spiralling inward and the southern companion growing more massive. In 1/4 orbit (5th panel from the left), the masses of the triple system are  $0.009 M_{\odot}$  (eastern),  $0.022 M_{\odot}$  (western), and  $0.029 M_{\odot}$  (primary). The western massive companion continues to accrete and becomes equal mass with the central primary ( $0.030 M_{\odot}$ ). The lighter companion is tidally stretched when it rotates in between the two massive objects; it is eventually merged onto the western companion to form a  $0.036 M_{\odot}$  secondary, the same

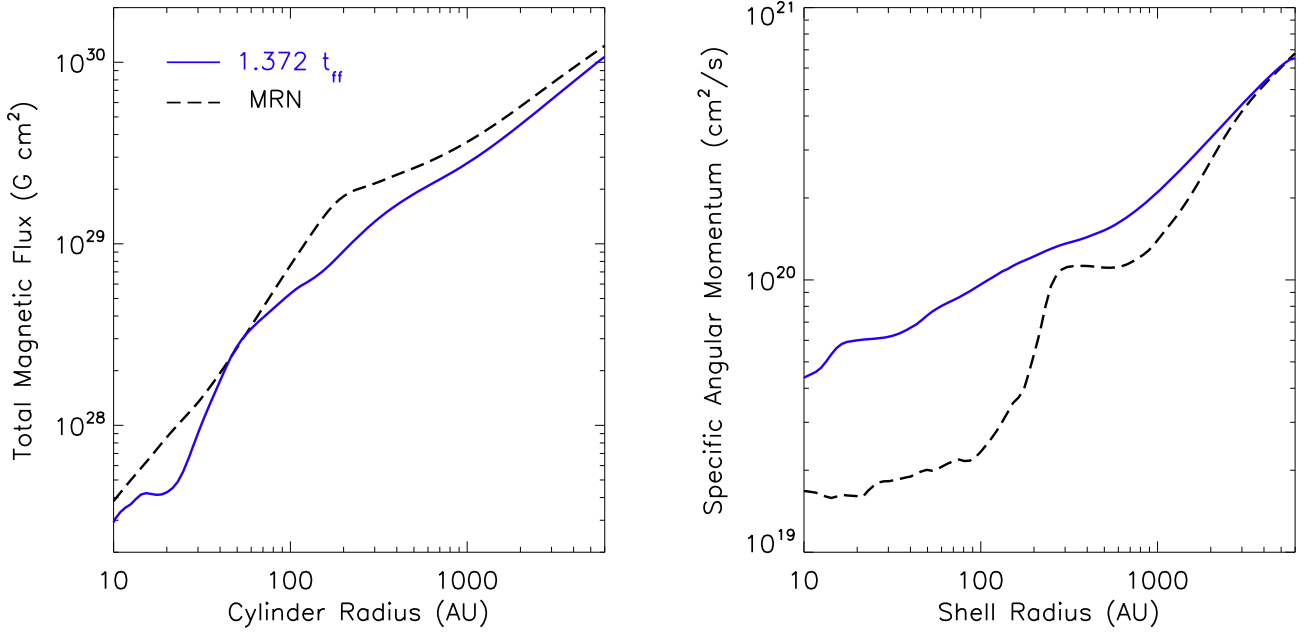


**Figure 10.** Total magnetic flux inside cylinders of different radii (left), and specific angular momentum inside shells at different radii (right), for the 2.4Slw-trMRN model at  $1.372t_{\text{ff}}$  and the 2.4Slw-MRN model at  $1.487t_{\text{ff}}$ . The two chosen frames have a similar total mass of star plus disc.

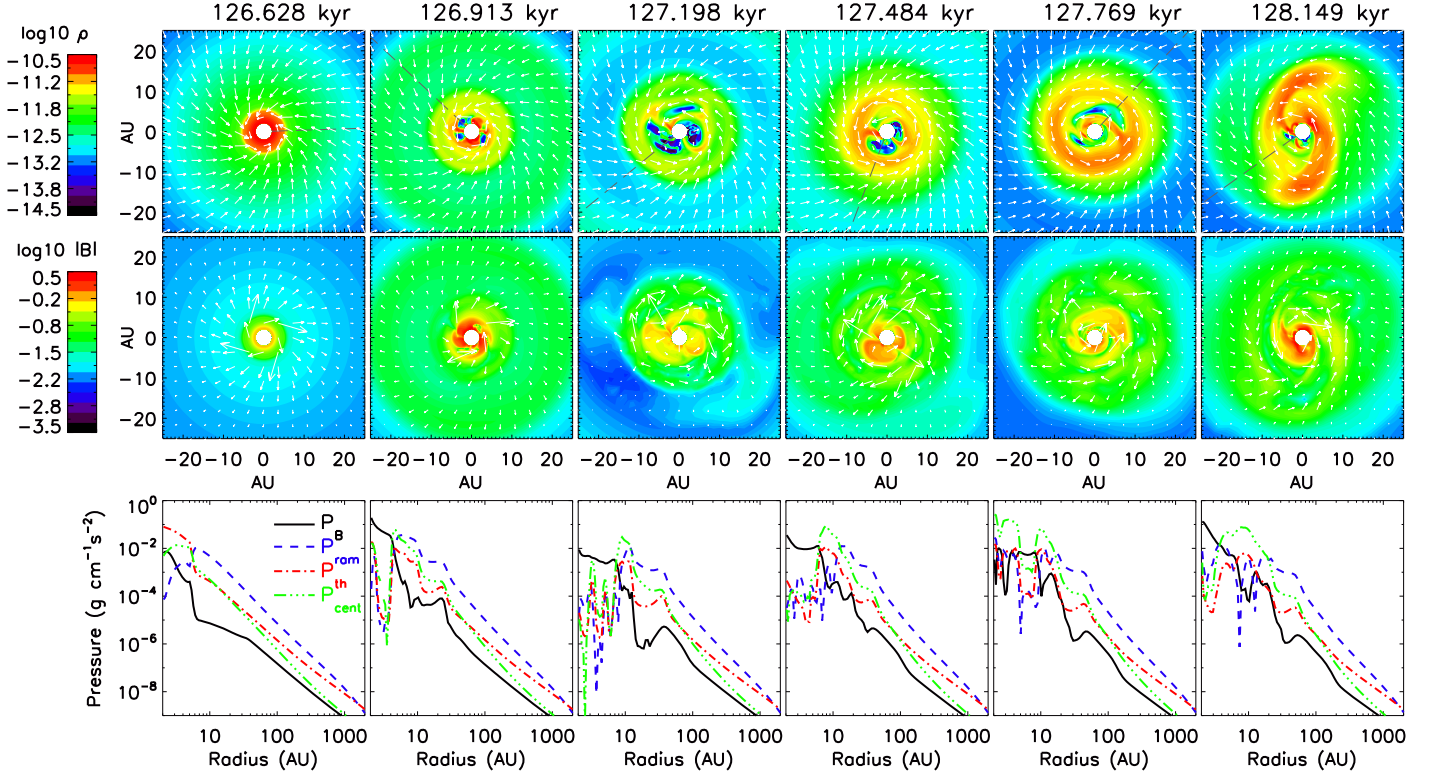


**Figure 11.** Early evolution of disc and DEMS for 2.4Slw-trMRN model. Top row: distribution of mass density  $\rho$  ( $\text{g cm}^{-3}$ ) and velocity field vectors within  $0.336^\circ$  of the equator. Middle row: distribution of magnetic field strength  $|B|$  and magnetic field vectors on the same surface. Bottom row: thermal  $P_{\text{th}}$ , magnetic  $P_{\text{B}}$ , ram  $P_{\text{ram}}$ , and effective centrifugal  $P_{\text{cent}}$  pressures along the same surface; the line cuts are drawn from the origin and pass through the low-density DEMS, with azimuthal angle  $\phi=1.9^\circ, 137^\circ, 219^\circ, 249^\circ, 47^\circ,$  and  $216^\circ$ , respectively (black dashed lines in the top row).

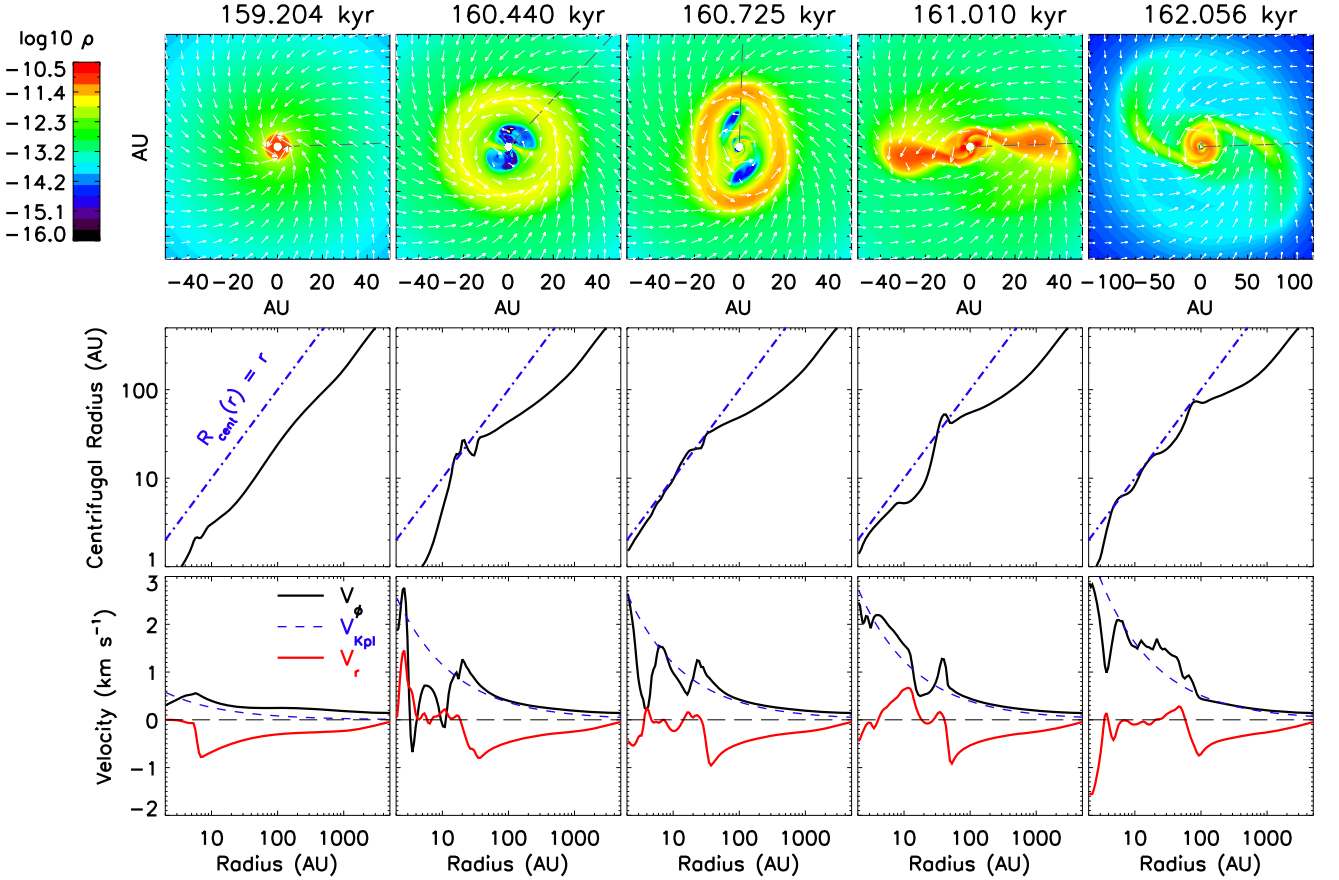


**Figure 12.** Early evolution of spiral structures for 2.4Fst-trMRN model. Top row: distribution of mass density  $\rho$  ( $\text{g cm}^{-3}$ ) and velocity field vectors within  $0.336^\circ$  of the equator. Middle row: estimated centrifugal radius. Bottom row: velocity profile along the same surface; the line cuts are drawn from the origin with azimuthal angle  $\phi=1.9^\circ, 47^\circ, 88^\circ, 1.9^\circ$ , and  $1.9^\circ$ , respectively (black dashed lines in the top row).

mass as the primary star (6th panel from the left). The secondary later merges with the primary and leads to another accretion burst; however, since we do not have full sink particle treatment (except for the stationary sink hole in the centre), the result could otherwise be a tight binary system with mass ratio  $\sim 1$  or a hierarchical triple system (Reipurth et al. 2014).

Throughout the evolution, the location of centrifugal barrier moves outward with time (middle row of Fig. 14), which matches with the radius of the large ring structure well. A second “plateau” also appears at 10 AU scale, corresponding to the centrifugally supported inner disc around the primary. Similar to the 4.8Slw-trMRN model above, the curves of centrifugal radius interior to the barrier are affected by the companion objects. The velocity profiles are plotted along lines passing through the companion objects, which show the usual “bump” feature in  $v_\phi$  and sudden decrease in  $v_r$  for a typical centrifugal barrier. Again, it confirms that the most probable sites for the formation of companion objects are the centrifugal barriers where the infall material piles up.

### 3.3.d Disc Stability Analysis

We conclude the section with a general analysis of disc stability. Recall that the criterion  $Q < 1$  only implies the growth of spiral waves in the disc. Indeed in Fig. 15, all four tr-MRN models satisfy the  $Q < 1$  criterion, yet only the two models with lower magneti-

zation ( $\lambda = 4.8$ ) show prominent fragmentation because the disc (or ring) is more massive and hence more unstable gravitationally. In these two models, new fragments often appear in the outer part of the spiral or ring structures, where infall material from the envelope piles up. In this sense, these piling-up spots are indeed the centrifugal barriers.

Interestingly, model 2.4Fst-trMRN and 4.8Slw-trMRN have very similar Toomre  $Q$  values at the early times, yet only the latter shows fragmentation. This is in fact consistent with the principles derived in Kratter et al. (2010) (see their Eq. 1–2 and Fig. 2). We compare the model 2.4Fst-trMRN at  $t = 162.1$  kyr (Fig. 12) and model 4.8Slw-trMRN at  $t = 113.4$  kyr (Fig. 13), both having a stellar mass of  $\sim 0.03 M_\odot$ . While both discs have similar accretion rate ( $\sim 10^{-5} M_\odot/\text{yr}$ ) and hence similar thermal parameter  $\zeta$ ,<sup>8</sup> the rotation speed of the spiral structure (not the envelope) in the 4.8Slw-trMRN model (tighter spiral) is twice faster than in the 2.4Fst-trMRN model (grand spiral). Accordingly, the 4.8Slw-trMRN model has a smaller rotational parameter  $\Gamma$ ,<sup>8</sup> which makes fragmentation easier according to Fig. 2 of Kratter et al. (2010). In other words, faster rotation (of the disc-spiral structure) promotes fragmentation.

<sup>8</sup>  $\zeta$  and  $\Gamma$  are dimensionless parameters used in Kratter et al. (2010).

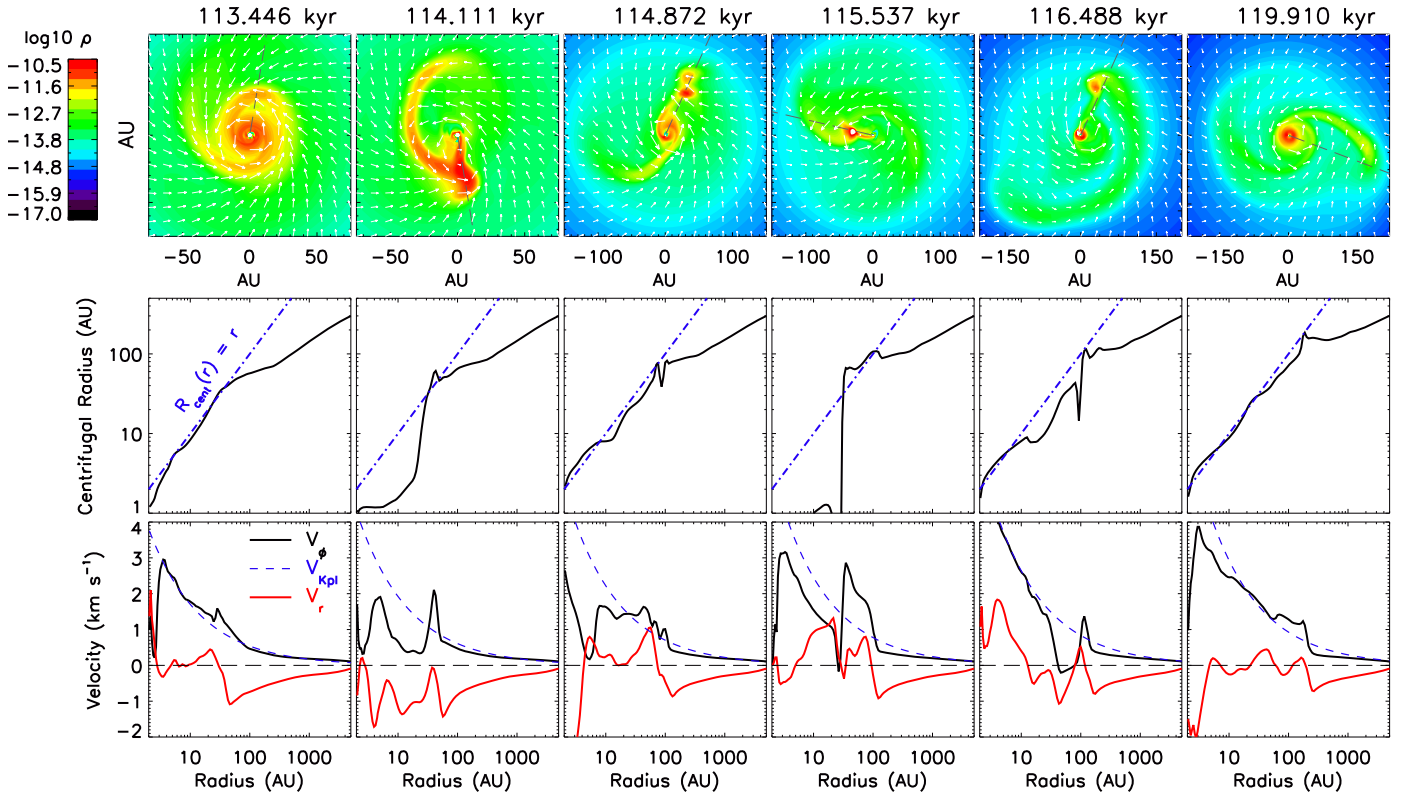


**Figure 13.** Evolution of spiral structures for 4.8Slw-trMRN model. Top row: distribution of mass density  $\rho$  ( $\text{g cm}^{-3}$ ) and velocity field vectors within  $0.336^\circ$  of the equator. Middle row: estimated centrifugal radius. Bottom row: velocity profile along the same surface; the line cuts are drawn from the origin with azimuthal angle  $\phi=81^\circ, 279^\circ, 66^\circ, 167^\circ, 66^\circ,$  and  $339^\circ$ , respectively (black dashed lines in the top row).

### 3.4 Failed Disc: Shrinking Disc

In Table 1, the 4.8Fst-MRN model is of particular interest, in which a 10–20 AU RSD forms initially but shrinks over time and disappears within  $\sim 3.7$  kyr. The same case has been discussed in our 2D study Zhao+16 (see their Section 5.4). Despite the advantage of weaker magnetization and faster rotation, the AD in the envelope is much less efficient than the tr-MRN models. As a result, an increasing amount of magnetic flux is being dragged into the inner disc forming region as collapse continues. The magnetic braking in this case still operates efficiently to torque down the gas rotation, leading to an insufficient supply of specific angular momentum to maintain the current disc size. Therefore, the RSD shrinks in size and the disc material gradually falls into the central star due to a lack of rotational support.

As shown in Fig. 17, the early evolution of the 4.8Fst-MRN model is similar to the tr-MRN models: DEMS “hatches” in the inner  $\sim 10$  AU after disrupting the first core; and a RSD assembles between 10–20 AU (2nd panel from the left). The unstable ring-shaped RSD then deforms and wraps around the star to form the usual disc-spiral configuration. However, in contrast to the large spirals in the tr-MRN models, the spiral structure in this case quickly disappears within  $\sim 600$  yr, leaving only a compact disc of 10–15 AU radius (4th panel from the left). The suppression of spiral structures is a sign of reduced angular momentum influx. Notably, in the next  $\sim 500$  yr, the infall flow gradually moves away from the equatorial plane, making the pseudo-disc to curve towards the upper hemisphere (recall that a similar phenomenon appears in the 2.4Slw-trMRN model as well).

It is a natural outcome of the low angular momentum in the infalling gas; the gas flow finds alternative channels to reach their centrifugal radius that is much smaller than the disc radius. In this fashion, the disc accretes mass but little angular momentum, which causes the disc to shrink in size over time.

The change of disc radius can also be identified from the evolution of centrifugal radius, particularly the secondary “plateau” for the inner tens of AU radius. Across different times, the value of  $R_{\text{cent}}$  indicated by the secondary “plateau” well follows the disc radius. It first increases from  $\sim 5$  AU to  $\sim 20$  AU at early times (1st–3rd panels from the left), but later decreases from  $\sim 10$  AU (4th panel from the left) to  $\sim 3$  AU (5th panel from the left) and quickly vanishes in another 200 yr (6th panel from the left). The lack of the inner “plateau” denotes the absence of RSD, which is exactly the case in the top row. At this time, the central region is instead occupied by the familiar DEMS.

In this 4.8Fst-MRN model, the initial advantage in rotation and magnetization provides sufficient angular momentum for the disc growth at early times; however, it is gradually taken over by the disadvantage in field decoupling in the envelope which determines the strength of magnetic braking in the disc forming region. We hereby compare this shrinking-disc model — 4.8Fst-MRN with the steady RSD model — 2.4Slw-trMRN (§ 3.1.a). Recall that the latter model has a stronger magnetization and a slower rotation, but no VSGs. At a similar evolutionary stage for the two models (similar total mass of star plus disc), Fig. 18 shows the specific angular momentum and magnetic torque for spherical shells at different radii. Here, we consider only the magnetic tension term while computing

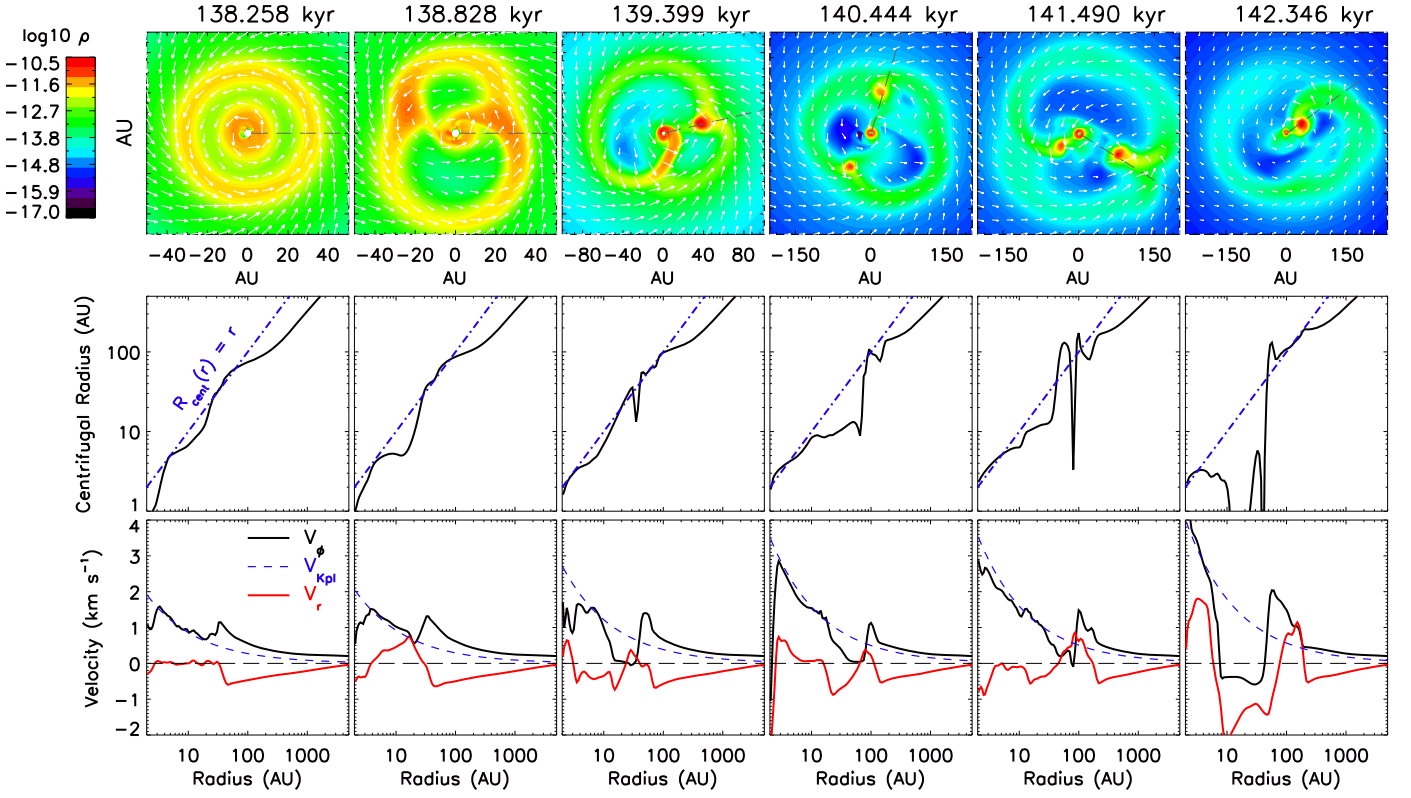


**Figure 14.** Evolution of spiral and ring structures for model 4.8Fst-trMRN. Top row: distribution of mass density  $\rho$  ( $\text{g cm}^{-3}$ ) and velocity field vectors within  $0.336^\circ$  of the equator. Middle row: estimated centrifugal radius. Bottom row: velocity profile along the same surface; the line cuts are drawn from the origin with azimuthal angle  $\phi=1.9^\circ, 1.9^\circ, 13^\circ, 73^\circ, 328^\circ$ , and  $36^\circ$ , respectively (black dashed lines in the top row).

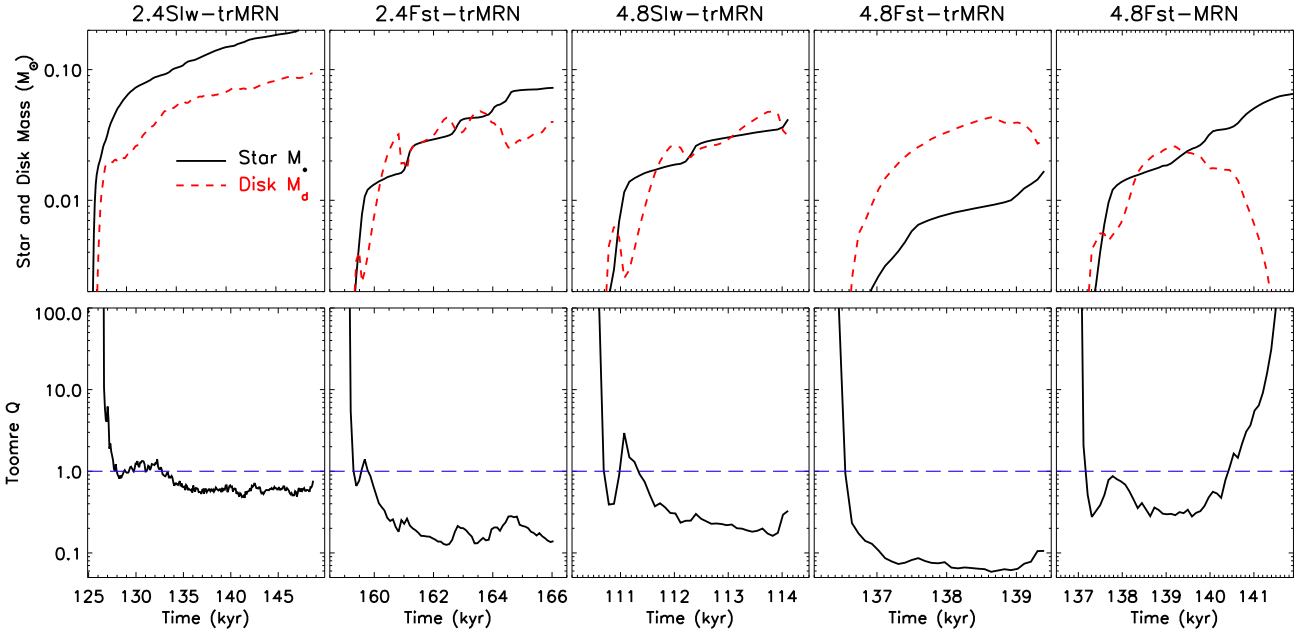


**Figure 15.** Evolution of mass of star and disc (top row), and Toomre  $Q$  (bottom row) for models with prominent discs. Dashed blue lines represent  $Q = 1$ . For models with formation of companion objects, 4.8Slw-trMRN and 4.8Fst-trMRN, we only show the quantities before the formation of companions.

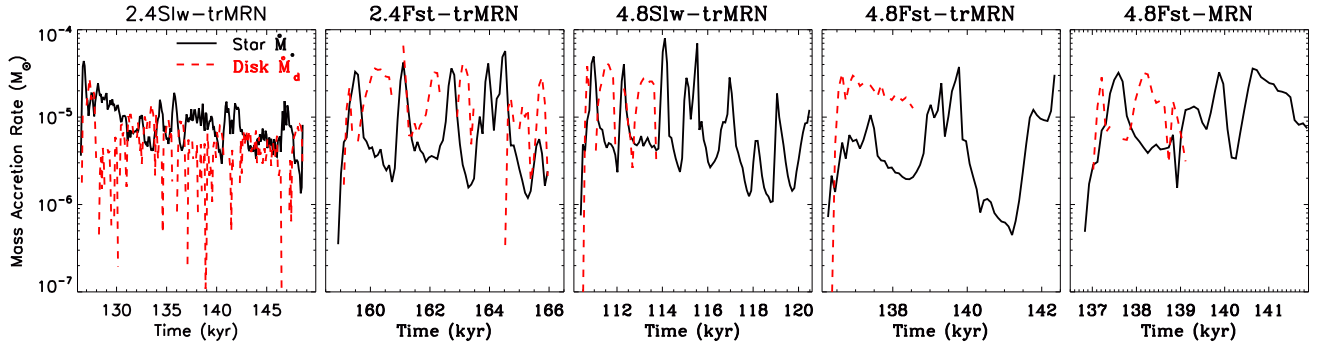


**Figure 16.** Evolution of mass accretion rate of the star and disc for models with prominent discs. In comparison to Fig. 15, we also show  $\dot{M}_*$  at later times for model 4.8Slw-trMRN and 4.8Fst-trMRN after the formation of companion objects.

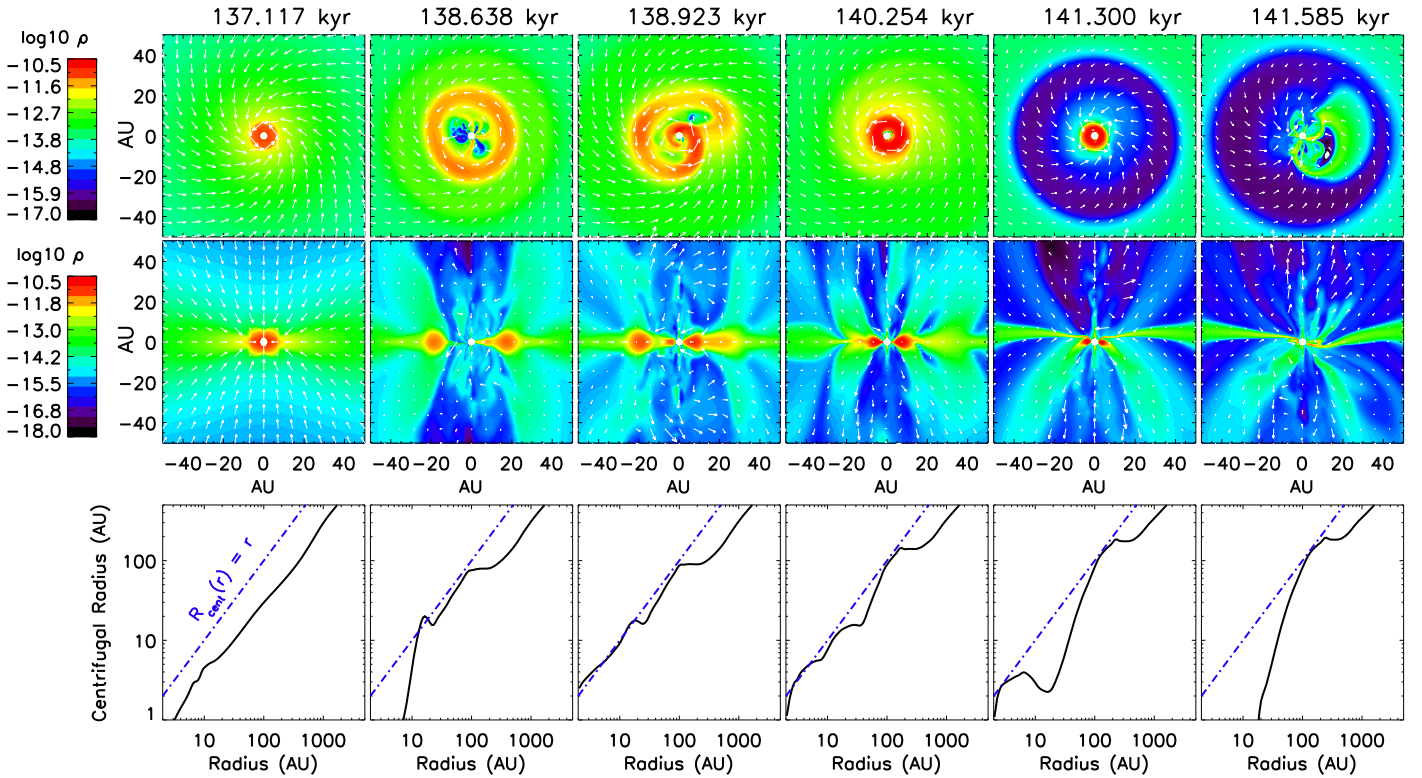


**Figure 17.** Evolution of the shrinking disc for model 4.8Fst-MRN. Top row: distribution of mass density  $\rho$  ( $\text{g cm}^{-3}$ ) and velocity field vectors within  $0.336^\circ$  of the equator. Middle row: distribution of mass density  $\rho$  ( $\text{g cm}^{-3}$ ) and velocity field vectors on the meridian plane with azimuthal angle  $\phi=1.9^\circ$ . Bottom row: estimated centrifugal radius.

the magnetic torque:

$$\mathcal{N}_t(S) = \frac{1}{4\pi} \int_S (\mathbf{r} \times \mathbf{B})(\mathbf{B} \cdot d\mathbf{S}) \quad (7)$$

(Zhao+16), where  $S$  is the shell surface at radius  $r$ . The contribution of the magnetic pressure term is generally much smaller (Matsumoto & Tomisaka 2004).

The magnetic torque in the 4.8Fst-MRN case peaks between 200–300 AU, near which the specific angular momentum curve flattens (conservation of angular momentum; Goodman et al. 1993; Belloche 2013). It implies that the magnetic torque is enhanced by

the increasing rotational motion there. The magnitude of magnetic torque in the 4.8Fst-MRN case is also a few times higher than the 2.4Slw-trMRN case, indicating a stronger magnetic braking in the former. Consequently, the specific angular momentum inside  $\sim 200$  AU decreases more rapidly in the MRN model. Such a quick slowing down in gas rotation in turn weakens the magnetic braking. In contrast, the strength of magnetic braking keeps at a relatively low level throughout the core. As a result, the decrease in specific angular momentum is more gradual. Even in the inner tens of AU, there is still an adequate amount of angular momentum to maintain



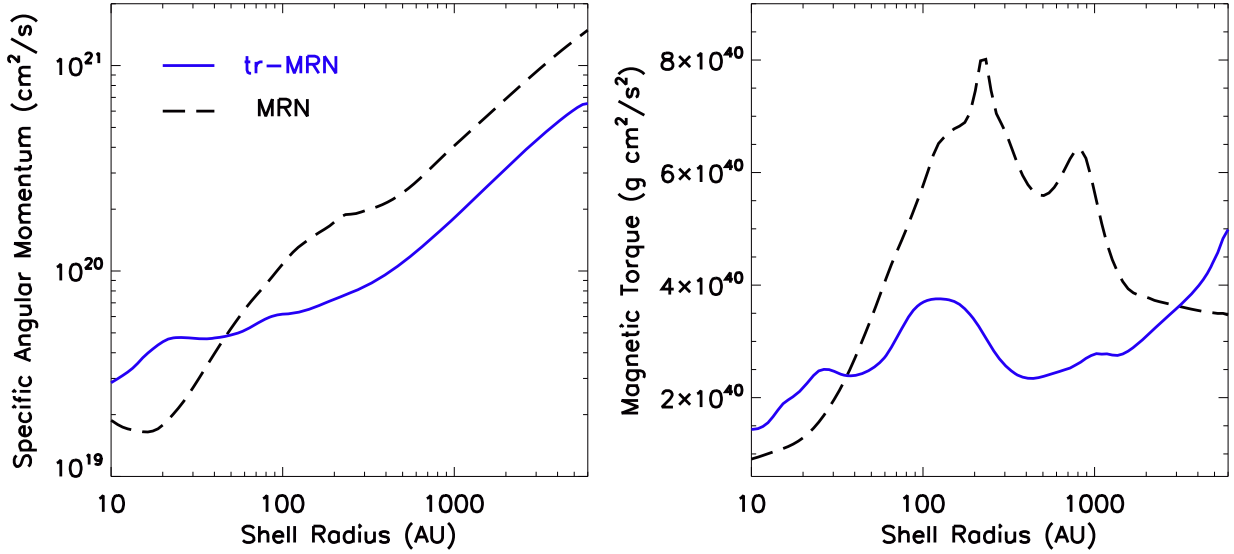


**Figure 18.** Comparison of specific angular momentum and magnetic torque for 4.8Fst-MRN and 2.4Slw-trMRN models at a similar evolutionary epoch 141.3 kyr and 128.5 kyr, respectively. The two chosen frames have similar total mass of star plus disc ( $\sim 0.06 M_{\odot}$ ).

the RSD. Therefore, the effect of removing VSGs is more significant on maintaining a long-lived RSD than that of increasing the initial core rotation or mass-to-flux ratio (for  $\lambda$  of a few).

### 3.5 Outflow

The formation and evolution of RSDs are naturally accompanied by magnetically-driven outflows. However, most outflows in our 3D models have multiple components, some of which can be asymmetric. Thus, different launching mechanisms may be in play for different outflow components. Note that we use an Alfvén  $d_t$  floor<sup>9</sup> to avoid extremely small timesteps, which may artificially add tiny mass to the outflow regions and can alter the momentum of the outflow. Therefore, the discussion in this section is more qualitative than quantitative.

As shown in Fig. 19, the outflow in the 2.4Slw-trMRN model has two components: one is centrally collimated and the other fanning out sideways. The former bipolar component may correspond to the jet or “X-wind” type (Shu et al. 2000); yet simulations with much higher resolution are required to understand its nature, which is beyond the scope of this study. The latter fan-like component, however, only appears in the upper hemisphere (similar to the 4.8Fst-MRN model). The origin of this outflow component is likely to be the magneto-centrifugal (‘slingshot’) mechanism (Blandford & Payne 1982), in that its launching point coincides with the landing site of the ‘curved’ infall stream, where magnetic field lines are strongly pinched. The bottom row of the 1st panel from the left

clearly shows that the pinching locations of magnetic field lines are shifted towards the upper hemisphere, following the curved infall stream. Therefore, the pseudo-disc is also curved instead of a plane along the equator. Note that the edge-on picture is very similar to the shrinking disc model (4.8Fst-MRN) discussed above, except that the landing site of the infall stream is at  $\sim 10$  AU compared with  $\lesssim 3$  AU in the shrinking disc model, thanks to the high angular momentum influx in the absence of VSGs.

In the other three tr-MRN models, the outer fan-like component of the outflow is not as prominent as the 2.4Slw-trMRN model; while the inner collimated component is clearly visible. The reason can be numerical (Alfvén  $d_t$  floor) as well as physical. As shown in the bottom rows of 2nd–4th panels from the left, magnetic field lines indeed pile up at the centrifugal barrier, which is in the form of spiral (2nd–3rd panels from the left) or ring (4th panel from the left) structures (see corresponding frames in Fig. 12–14). However, the “ring type” centrifugal barrier show more obvious fan-like outflow cavities than the “spiral type” centrifugal barrier; this is because the former barrier is more efficient in blocking infall and piling up field lines, while the spiral structure still allow materials and field lines to further fall and spiral along it. Nevertheless, the fan-like outflow should be visible if the accretion flow from the envelope lands on a narrow region of the disc or ring, which can be an explanation to the outflow offset recently observed by Bjerkeli et al. (2016) and Alves et al. (2017). In this paradigm, asymmetric (one-sided) outflows can be more common than symmetric ones.

## 4 DISCUSSION

### 4.1 DEMS & AD Shock

The main difference of our work with previous studies is the relatively efficient decoupling of magnetic field in the collapsing envelope. It not only promotes the formation of RSDs, but also avoids the abrupt decoupling of the large amount of magnetic flux dragged into

<sup>9</sup> The minimum density allowed for any given cell is set to  $\frac{|B|^2}{4\pi(|\Delta x|_{\min}/d_{t_{\text{floor, Alfvén}}})^2}$ , where  $|\Delta x|_{\min}$  is the smallest of the cell’s sizes along  $r$ ,  $\theta$ , and  $\phi$  directions, and  $d_{t_{\text{floor, Alfvén}}}$  is set to  $3 \times 10^5$  seconds. As a result, artificial mass is added to cells with densities below the minimum density. Such a floor usually triggers in the bipolar regions with very large Alfvén speeds and often very tiny  $|\Delta x|_{\phi}$ .

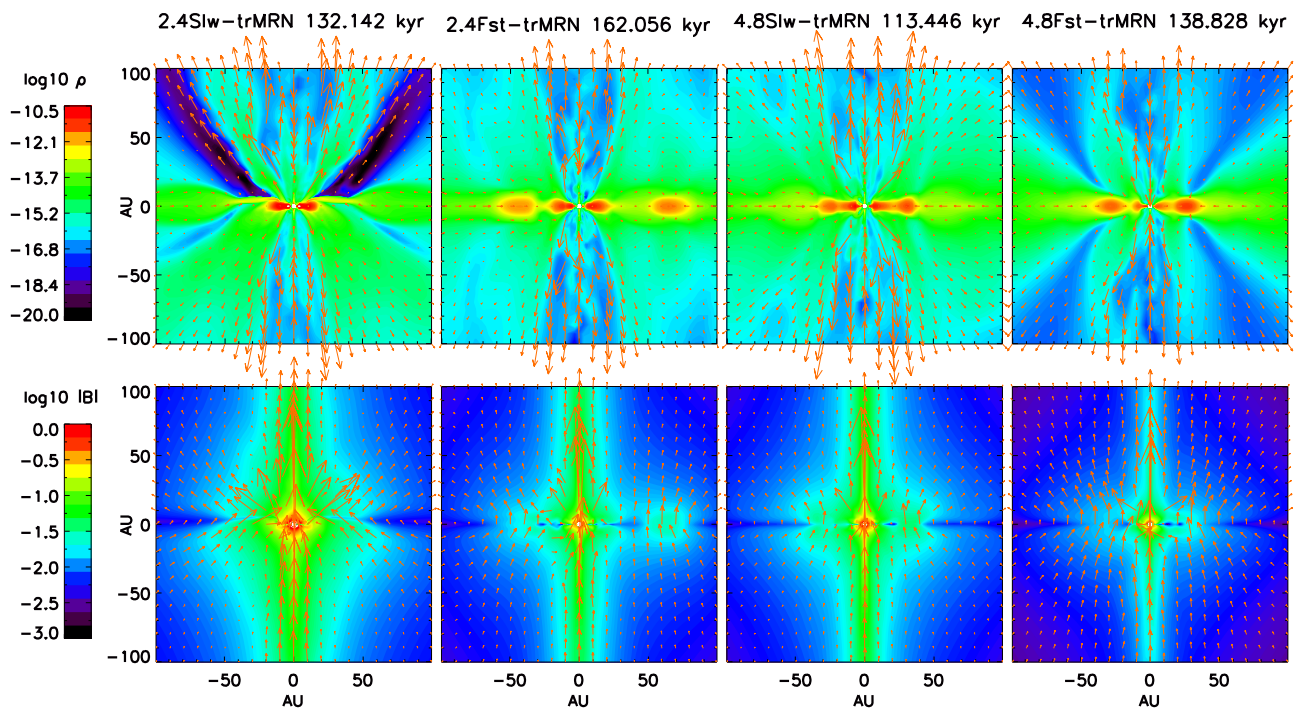


**Figure 19.** Comparison of outflow structures in the bipolar region (top row) and magnetic field configurations (bottom row) among the disc forming models. The colour contours are logarithmic mass density  $\rho$  ( $\text{g cm}^{-3}$ ) and magnetic field strength  $|B|$  (G) for top and bottom rows, respectively. The red arrows are velocity field and magnetic field vectors on the meridian plane for the top and bottom rows, respectively.

the stellar vicinity. Otherwise, as we have demonstrated in models with MRN grains, sooner or later, DEMS will dominate the inner tens to hundreds of AU regions, obstructing the gas rotation further. Similarly, if efficient AD only occurs in the inner tens of AU, the “so-called” AD-shock (Li & McKee 1996) is also inevitable. Therefore, the magnetic flux problem and magnetic braking catastrophe in star formation are closely related. Averting the former will simultaneously alleviate the latter, which can be achieved by the removal of VSGs in the collapsing protostellar envelope or even earlier, during the prestellar core.

## 4.2 Disc Size

Among the tr-MRN models, the inner RSDs (or circumstellar discs) at later times are of  $\sim 20$  AU in radius and are surrounded by the extended spiral structures. This picture seemingly matches the self-regulated disc formation model by Hennebelle et al. (2016). However, even the non-magnetic models (Table 1) produce small circumstellar discs with  $\sim 20$  AU radius; yet their rotation-dominated spiral structures are much larger. Hence, the small disc radius is unlikely to result from magnetic effects. In fact, the size of the circumstellar disc is mainly determined by the thermal support (Fig. 20) and is sensitive to the adiabatic index (see Appendix A). In comparison, the extended spiral structures are as thick as 100–150 AU in the vertical direction and are not in hydrostatic equilibrium at large scale heights; the outer layers are largely infalling towards the midplane. Therefore, the extended spiral structure may not be strictly defined as part of the disc, but a transition zone between the envelope and the circumstellar disc, where infalling gas starts to spiral inward. Furthermore, when considering the magnetic flux distribution during the collapse, the dominant term should be  $\frac{\partial B_r}{\partial z}$ , i.e., field pinching

along the infall plane as we have shown in §. 3.1.c, instead of  $\frac{\partial B_z}{\partial r}$  considered in Hennebelle et al. (2016).

The main difference between the non-magnetic and magnetic models is the size of the spiral structure, which is much larger in the non-magnetic models (Table 1). The spiral structure marks the regions where rotation starts to dominate over infall (hints of large spiral structures in recent observations: Tokuda et al. 2014, Pérez et al. 2016, and Yen et al. 2017). Thus, the outer edge of the spiral structure is generally the location where the specific angular momentum curve starts to flatten (Goodman et al. 1993; Belloche 2013, e.g.), or the plateau of the centrifugal radius curve. Because of the quickening of rotational motion, the magnetic braking is also the strongest inside the spiral regions (e.g., Fig. 18), which makes the spiral structure smaller over time in models with stronger magnetic field.

## 4.3 Lower Limit for $\beta_{\text{rot}}$ & The Case of B335

As we have shown that both initial rotation and magnetization can affect the formation of RSDs, we thus explore the lower limit of initial rotation speed below which an RSD is hard to form. From the test simulations we carried out for tr-MRN grains,<sup>10</sup> we find that, in order for discs to form, the ratio of rotational to gravitational energy  $\beta_{\text{rot}}$  should be higher than  $\sim 1.5$ – $1.6\%$  for initial magnetization of  $\lambda=2.4$  and  $\sim 0.5$ – $0.6\%$  for magnetization of  $\lambda=4.8$ , which corresponds to a lower limit of angular speed  $\omega_0=8 \times 10^{-14} \text{ s}^{-1}$

<sup>10</sup> The initial angular speed  $\omega_0$  tested includes  $8 \times 10^{-14} \text{ s}^{-1}$  and  $7.2 \times 10^{-14} \text{ s}^{-1}$  for initial magnetization of  $\lambda = 2.4$ , and  $6.4 \times 10^{-14} \text{ s}^{-1}$ ,  $5 \times 10^{-14} \text{ s}^{-1}$ , and  $4 \times 10^{-14} \text{ s}^{-1}$  for initial magnetization of  $\lambda = 4.8$ .

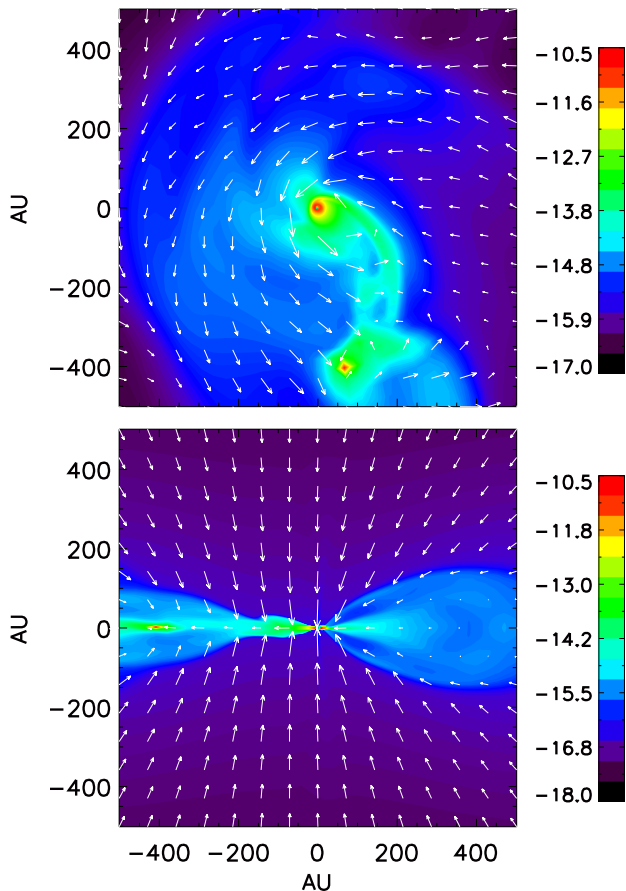


**Figure 20.** Binary system formed in the HydroSlw model at  $t \approx 119.5$  kyr, with the central object of  $0.087 M_{\odot}$ . Both circumstellar discs are  $\sim 10$ – $20$  AU in radius. The bulk part of the circumstellar disc has a temperature of  $50$ – $100$  K. The distribution of logarithmic mass density and vectors of velocity fields are plotted within  $0.336^{\circ}$  of the equator (top) and on the meridian plane (bottom).

and  $5 \times 10^{-14} \text{ s}^{-1}$  respectively. Note that these values only apply to dense cores with initial solid-body rotation profile.<sup>11</sup>

When the initial rotation is slower than the lower limit, the infalling gas will reach a centrifugal radius of  $<10$  AU, dragging a large amount of magnetic flux to the stellar vicinity (even under the enhanced AD due to removal of VSGs). Therefore, the central  $\sim 10$  AU region is inevitably dominated by DEMS, which constantly disrupt the disc structure and suppress the formation of a well-defined RSD. As shown in Fig. 21, the central object is surrounded by filamentary accretion streams rather than a disc (face-on view).

<sup>11</sup> The lower limit of  $\beta_{\text{rot}}$  found here is likely to be a key for the small disks ( $\leq 10$  AU) formed in Dapp et al. 2012, apart from their high cosmic-ray ionization rate ( $\zeta_0^{\text{H}_2} = 5.0 \times 10^{-17} \text{ s}^{-1}$ ). In Figure 2 of Dapp et al. 2012, they showed very similar trend of enhanced AD in the absence of VSGs as we presented in Zhao+16; however, they did not elaborate on its effect on disk formation. The initial rotation speed used in Dapp et al. (2012) as well as in Dapp & Basu (2010) ( $1 \text{ km s}^{-1} \text{ pc}^{-1} \approx 3.2 \times 10^{-14} \text{ s}^{-1}$ ) seems to be too slow to produce disks larger than 10 AU. It corresponds to  $\beta_{\text{rot}} \sim 0.6\%$  for their  $\lambda = 2$  core, which is well below the lower limit we found for the  $\lambda = 2.4$  case.

In the edge-on view, the infall stream curves towards the upper hemisphere and lands onto the disc from above, which results in an one-sided outflow (similar to the 2.4Slw-trMRN and 4.8Fst-MRN models above<sup>12</sup>). The curve of centrifugal radius decreases nearly monotonically towards the inner 10 AU, only showing a small plateau at  $\sim 5$  AU. It is consistent with the landing radius of the infall stream.

This particular model matches to some extent the observation of B335, where no Keplerian disc  $>10$  AU is found around the protostar (Yen et al. 2015b; Evans et al. 2015) yet CO outflows are clearly visible (Yen et al. 2010). The estimated angular speed of the host core is about  $2.6 \times 10^{-14} \text{ s}^{-1}$ , which is a few times lower than other protostellar sources with disc detection (Yen et al. 2015). This value is close to the lower limit of angular speed we find for  $\lambda = 4.8$  cores. It is likely that B335 is already in lack of VSGs during the collapse process; otherwise, a much larger angular speed ( $>10^{-13} \text{ s}^{-1}$ ) or mass-to-flux ratio ( $>10$ ) of the host core is required with the full MRN distribution to form even a small, short-lived (or shrinking) disc (§. 3.4). Nevertheless, a disc, even a small one, is necessary to power the ordered, wide-angle outflows observed in B335; a fully magnetically dominated inner region with no disc at all generally produces chaotic morphologies in the bipolar region, which is unlikely the case for B335.

#### 4.4 VSGs in Dense Cores

The lack of VSGs in dense cores (Tibbs et al. 2016) can be caused by either (1) grain evolution or (2) magnetic selection effect. The former includes accretion of VSGs onto grain mantles (process analogous to molecular freeze-out, e.g., Tielens & Hagen 1982; Hasegawa et al. 1992) and grain coagulation (Chokshi et al. 1993; Dominik & Tielens 1997); and the latter refers to the differential coupling of grains to the magnetic field based on their size (Ciolek & Mouschovias 1996). While grain evolution can start from the quiescent prestellar phase, magnetic selection normally occurs during the collapse phase. We will leave the more complete chemistry model including grain evolution and multi-fluid non-ideal MHD to future studies.

#### 4.5 Numerical Limitations

Finally, we raise cautions for the potential limitations of our numerical treatment.

*First*, we use Alfvén  $dt$  floor to limit the velocity of MHD waves, which will add tiny mass to certain grid cells with low density but strong magnetic field (the total added mass for the entire computational domain is on the order of  $\sim 10^{-3}$ – $10^{-2}$  of the central point mass). The floor is most likely to trigger in the bipolar regions, which can affect the outflow dynamics and more specifically, slowing down the outflow.

*Second*, we set an AD  $dt$  floor ( $dt_{\text{floor,AD}}$ ) to avoid intolerably small AD timesteps. The result is that the AD diffusivity  $\eta_{\text{AD}}$  is capped<sup>13</sup>

<sup>12</sup> In some test simulations, the infall stream can also curve towards the lower hemisphere and land onto the disc from below.

<sup>13</sup> The cap of  $\eta_{\text{AD}}$  is computed for each cell as  $\text{CFL}_{\text{AD}} \frac{|\Delta x|_{\text{min}}^2}{4 dt_{\text{floor,AD}}}$ , where  $\text{CFL}_{\text{AD}}=0.4$  is the Courant-Friedrichs-Lewy number for AD,  $|\Delta x|_{\text{min}}$  is the smallest of the cell's sizes along  $r$ ,  $\theta$  and  $\phi$  directions, and  $dt_{\text{floor,AD}}$  is set to  $3 \times 10^6$  seconds. Such an  $\eta_{\text{AD}}$  cap based on  $dt_{\text{floor,AD}}$  behaves approximately as a constant  $\eta_{\text{AD}}$  cap of  $\sim 10^{19} \text{ cm}^2 \text{ s}^{-1}$  in the bulk part of the circumstellar disc.

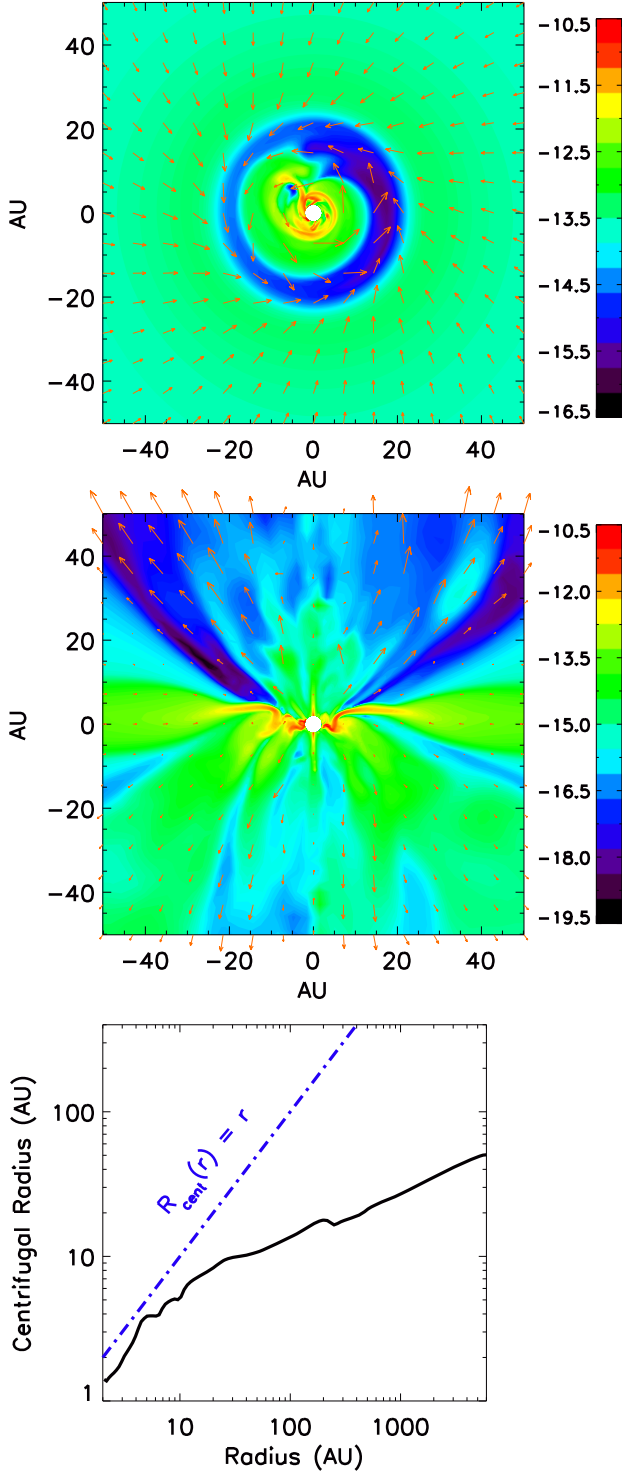


**Figure 21.** Distribution of logarithmic mass density  $\rho$  ( $\text{g cm}^{-3}$ ) within  $0.336^\circ$  of the equator (top) and on the meridian plane (middle) for a slow rotating core ( $\omega_0 = 4 \times 10^{-14} \text{ s}^{-1}$ ) with  $\lambda = 4.8$  at  $t \approx 107.9$  kyr. The mass of the central object is  $\sim 0.06 M_\odot$ . Orange vectors are velocity fields. The DEMS are constantly disrupting the disc structure ( $< 10$  AU) in the centre. Outflows are yet prominent. Bottom: estimated centrifugal radius.

in the outflow region and bulk part of the disc (if any), which causes the matter there to be better coupled to the magnetic fields than it should be. This cap on  $\eta_{\text{AD}}$  should not affect our main result that disc formation is enabled by ambipolar diffusion in the infalling envelope. We have explored smaller values of  $dt_{\text{floor,AD}}$  ( $= 1 \times 10^6$  and  $3 \times 10^5$ ) using a lower resolution in  $r$ -direction ( $\delta r = 0.33$  AU), and find that large DEMS still dominate the central regions around the star and disc formation is strongly suppressed as in § 3.1.b. Therefore, in terms of forming RSDs, the specific angular momentum of the infalling gas being accreted by the disc plays a dominant role over the decoupling process in the disc itself.

*Third*, the code has no sink particle treatment (except for the stationary sink hole in the centre), and hence is not ideal for following orbital evolution of binary and multiple systems. We only confirm the onset of fragmentation and the formation of companion stellar masses.

*Fourth*, we have not included Ohmic and Hall effect in this study, but their corresponding diffusivities are computed regardlessly. We found in the tr-MRN models the Ohmic diffusivity is about  $\sim 10$  times smaller than the ambipolar diffusivity inside the circumstellar discs. As we have shown in Zhao+16, Ohmic dissipation has negligible effect on disc formation because (1) with the full MRN distribution, the lack of dense long-lived disc in the first place makes it difficult for Ohmic dissipation to dominate; while (2) in the absence of VSGs, ambipolar diffusivity always dominates over Ohmic diffusivity at densities below  $10^{14}$ – $10^{15} \text{ cm}^{-3}$ . Once we further decrease the radius of the inner boundary (e.g. below 1 AU), the inclusion of Ohmic dissipation will become crucial. Besides, Hall effect is very sensitive to the polarity of magnetic field (Krasnopolsky et al. 2011; Braiding & Wardle 2012; Tsukamoto et al. 2015b; Wurster et al. 2016), which adds another twist to the formation of protostellar discs. We will investigate the interplay between the three non-ideal MHD effects in future studies.

## 5 SUMMARY

We have extended our 2D study of protostellar disc formation (Zhao+16) to 3D, using the same equilibrium chemical network. We have verified the main result found in Zhao+16 that the removal of VSGs enables the formation of RSDs of tens of AU through the enhanced ambipolar diffusion of magnetic fields in the collapsing envelope. Because of the reduction of magnetic flux dragged into the central disc forming region, magnetic braking becomes less efficient and the key ingredient for disc formation — *angular momentum* — is sufficiently retained. Further conclusions are listed below.

1. Collapse pinches magnetic field lines along the infall plane (pseudo-disc plane) where ambipolar drift is the strongest ( $\propto \frac{\partial B_r}{\partial \theta}$ ). With the enhanced  $\eta_{\text{AD}}$  (VSGs absent), the “effective” ion velocity (or the magnetic field velocity) nearly vanishes along the infall plane even at  $10^2$ – $10^3$  AU scales. This indicates that magnetic fields are gradually left behind in the envelope by the collapsing neutral matter.

2. The so-called DEMS (formed by the decoupled magnetic flux from the accreted matter) can still suppress disc formation and obstruct disc rotation if the full MRN distribution is used. Even in the absence of VSGs, DEMS are still present at early times. They play the role of disrupting the first core, preventing it from directly evolving into a circumstellar disc. Disc formation in such cases relies on the supply of high angular momentum material from the infalling envelope.

3. High specific angular momentum entering the inner region enables both the formation of RSDs and the development of spiral (or ring) structures. The size of spirals (or rings) matches the centrifugal radius of the infalling gas. The outer edge of the spirals (or rings) is also the location where the specific angular momentum curve starts to flatten.

4. When the initial core is relatively weakly magnetized (with a dimensionless mass-to-flux ratio of 4.8 rather than 2.4), fragmentation frequently occurs on the outer spiral arms (or on the rings), where infall material from the envelope piles up. Such fragments of tens of Jupiter mass could mark the early onset of multiple systems. Some of the fragments, particularly when the core rotation is relatively slow, merge quickly with the central stellar object, producing bursts of mass accretion. Others are longer lived, and can potentially survive as multiple stellar systems, although sink particles are needed to better follow their long-term evolution.

5. Magnetically-driven outflows have multiple components. The central bipolar component is more symmetric and collimated, which may correspond to jet or “X-wind”. The outer fan-like component can be more asymmetric (one-sided). Its launching location coincides with the landing site of the infalling gas on the disc or ring.

## ACKNOWLEDGEMENTS

We thank Kengo Tomida for providing the data of evolutionary track. BZ and PC acknowledge support from the European Research Council (ERC; project PALs 320620). Z.-Y. L. is supported in part by NASA NNX14AB38G, NSF AST-1313083, and NSF AST-1716259. Numerical simulations are carried out on the CAS group cluster at MPE.

## APPENDIX A: EQUATION OF STATE

We use a broken power law profile for the equation of state (EOS), fitted to mimic the radiative transfer results of Tomida et al. (2013):

$$T = \begin{cases} T_0 + 1.5 \frac{\rho}{10^{-13}} & \text{for } \rho < 10^{-12} \\ (T_0 + 15) \left( \frac{\rho}{10^{-12}} \right)^{0.6} & \text{for } 10^{-12} \leq \rho \leq 10^{-11} \\ 10^{0.6} (T_0 + 15) \left( \frac{\rho}{10^{-11}} \right)^{0.44} & \text{for } 10^{-11} \leq \rho \leq 3 \times 10^{-9} \end{cases} \quad (\text{A1})$$

where  $T_0 = 10$  K. The comparison for different EOS is shown in Fig. A1. The conventional 5/3 law reproduces the right slope below  $10^{-11}$  g cm<sup>-3</sup> but overestimates the gas pressure by a factor of  $\sim 2$ , while the 7/5 law reproduces the right slope beyond  $10^{-11}$  g cm<sup>-3</sup> but underestimates the gas pressure by a factor of  $\sim 2$ . As a result, the usual 5/3 law tends to form thermally supported structures with somewhat larger sizes, while the structures formed by the 7/5 law are smaller and vulnerable to gravitationally compression. Note that the density regime which matters the most for disc formation is below  $10^{-11}$  g cm<sup>-3</sup> (Zhao et al. 2016), hence the 5/3 power law provides better thermal stability than the 7/5 profile.<sup>14</sup>

<sup>14</sup> We find that stiffening the EOS at  $3 \times 10^{-13}$  g cm<sup>-3</sup> offers a more realistic thermal pressure than at  $1 \times 10^{-13}$  g cm<sup>-3</sup> for the single 5/3 power law.

## REFERENCES

- Allen, A., Li, Z.-Y., & Shu, F. H. 2003, ApJ, 599, 363  
 Alves, F. O., Girart, J. M., Caselli, P., Franco, G. A. P., Zhao, B., Vlemmings, W. H. T., Evans, M. G., & Ricci, L. 2017, A&A, 603, 3  
 Basu, S., & Mouschovias, T. Ch. 1994, ApJ, 432, 720  
 Bate, M. R. 1998, ApJ, 508, 95  
 Bate, M. R. 2010, MNRAS, 404, 79  
 Bate, M. R. 2011, MNRAS, 417, 2036  
 Bergin, E. A., & Tafalla, M. 2007, ARA&A, 45, 339  
 Belloche, A. 2013, EAS, 62, 25  
 Bjerkeli, P., van der Wiel, M. H. D., Harsono, D., Ramsey, J. P., & Jørgensen, J. K. 2016, Nature, 540, 406  
 Blandford, R. D., & Payne, D. G. 1982, MNRAS, 199, 883  
 Braiding C. R., & Wardle M. 2012, MNRAS, 422, 261  
 Chokshi, A., Tielens, A. G. G. M., & Hollenbach, D. 1993, ApJ, 407, 806  
 Ciolek, G. E., & Mouschovias, T. Ch. 1996, ApJ, 468, 749  
 Codella, C., Cabrit, S., Gueth, F., Podio, L., Leurini, S., Bachiller, R., Gusdorf, A., Lefloch, B., Nisini, B., Tafalla, M., & Yvart, W. 2014, A&A, 568, 5  
 Dapp, W. B., & Basu, S. 2010, A&A, 521, 56  
 Dapp, W. B., Basu, S., & Kunz, M. W. 2012, A&A, 541, 35  
 Dominik, C. & Tielens, A. G. G. M. 1997, ApJ, 480, 647  
 Evans, N. J., II, Di Francesco, J., Lee, J.-E., Jørgensen, J. K., Choi, M., Myers, P. C., & Mardones, D. 2015, ApJ, 814, 22  
 Galli, D., & Shu, F. H. 1993, ApJ, 417, 243  
 Goodman, A. A., Benson, P. J., Fuller, G. A., & Myers, P. C. 1993, ApJ, 406, 528  
 Hasegawa, T. I., Herbst, E., & Leung, C. M. 1992, ApJS, 82, 167  
 Hennebelle, P., Commerçon, B., Chabrier, G., & Marchand, P. 2016, ApJ, 830, 8  
 Hirashita, H. 2012, MNRAS, 422, 1263  
 Joos, M., Hennebelle, P., & Ciardi, A. 2012, A&A, 543, 128  
 Kaisig, M., Tajima, T., & Lovelace, R. V. E. 1992, ApJ, 386, 83  
 Kim, W., & Ostriker, E. C. 2001, ApJ, 559, 70  
 Köhler, M., Stepnik, B., Jones, A. P., Guillet, V., Abergel, A., Ristorcelli, I., & Bernard, J.-P. 2012, A&A, 548, 61  
 Königl, A. 1987, ApJ, 320, 726  
 Krasnopolsky, R., & Königl, A. 2002, ApJ, 580, 987  
 Krasnopolsky, R., Li, Z.-Y., & Shang, H. 2010, ApJ, 716, 1541  
 Krasnopolsky, R., Li, Z.-Y., & Shang, H. 2011, ApJ, 733, 54  
 Krasnopolsky, R., Li, Z.-Y., Shang, H., & Zhao, B. 2012, ApJ, 757, 77  
 Kratter, K. M., Matzner, C. D., Krumholz, M. R., & Klein, R. 2010, ApJ, 708, 1585  
 Kratter, K. M., & Lodato, G. 2016, ARA&A, 54, 271  
 Kunz, M. W., & Mouschovias, T. Ch. 2009, ApJ, 693, 1895  
 Kunz, M. W., & Mouschovias, T. Ch. 2010, MNRAS, 408, 322  
 Larson, R. B. 1969, MNRAS, 145, 271  
 Lee, C.-F., Li, Z.-Y., Ho, P. T. P., Hirano, N., Zhang, Q., & Shang, H. 2017, Science Advances, 3, e1602935  
 Lewis, B. T., & Bate, M. R. 2017, MNRAS, 467, 3324  
 Li, Z.-Y., & McKee, C. F. 1996, ApJ, 464, 373  
 Li, Z.-Y., Krasnopolsky, R., & Shang, H. 2011, ApJ, 738, 180  
 Li, Z.-Y., Krasnopolsky, R., Shang, H., & Zhao, B. 2014, ApJ, 793, 130  
 Mac Low, M.-M., Norman, M. L., Königl, A., & Wardle, M. 1995, ApJ, 442, 726  
 Machida, M. N., & Matsumoto, T. 2011, MNRAS, 413, 2767  
 Masson, J., Chabrier, G., Hennebelle, P., Vaytet, N., & Commerçon, B. 2015, A&A, 587, 32  
 Matsumoto, T., & Tomisaka, K. 2004, ApJ, 616, 266  
 Mellon, R. R., & Li, Z.-Y. 2008, ApJ, 681, 1356  
 Mellon, R. R., & Li, Z.-Y. 2009, ApJ, 698, 922  
 Mestel, L., & Spitzer, L., Jr. 1956, MNRAS, 116, 503  
 Mouschovias, T. Ch. 1977, ApJ, 211, 147  
 Mouschovias, T. Ch., & Paleologou, E. V. 1980, ApJ, 237, 877  
 Mouschovias, T. Ch., & Paleologou, E. V. 1986, ApJ, 308, 781  
 Murillo, N. M., Lai, S.-P., Bruderer, S., Harsono, D., & van Dishoeck, E. F. 2013, A&A, 560, 103

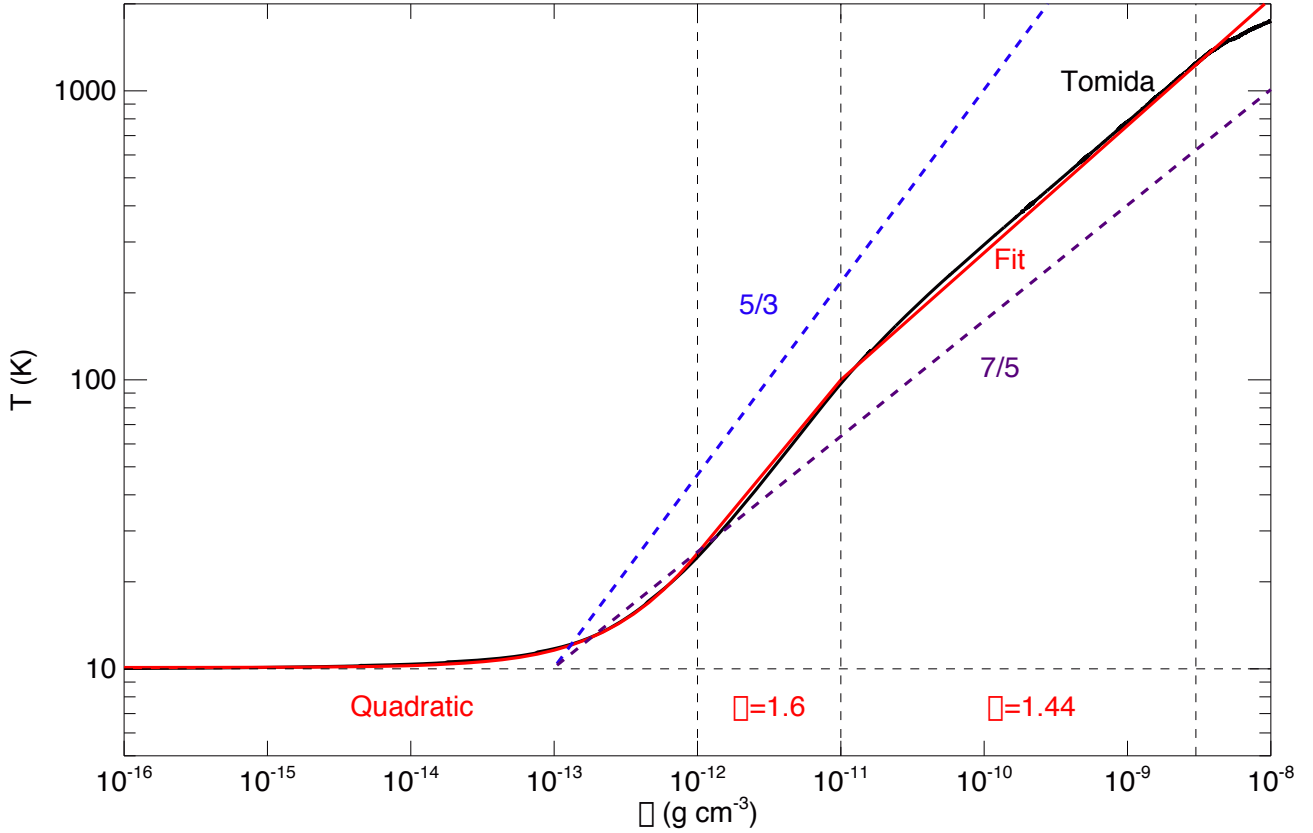


**Figure A1.** Function fitting (red solid curve) for the evolutionary track from Tomida et al. (2013) (black solid curve). The barotropic EOS with adiabatic indices of 5/3 and 7/5 are shown in blue dashed and purple dashed lines.

- Ossenkopf, V. 1993, *A&A*, 280, 617
- Parker, E. N. 1979, *Cosmical Magnetic Fields, Their Origin and Activity* (Oxford: Clarendon), chap. 15
- Pérez, L. M., Carpenter, J. M., Andrews, S. M., et al. 2016, *Science*, 353, 1519
- Pinto, C., & Galli, D. 2008, *A&A*, 484, 17
- Reipurth, B., Clarke, C. J., Boss, A. P., Goodwin, S. P., Rodríguez, L. F., Stassun, K. G., Tokovinin, A., & Zinnecker, H. 2014, *Protostars and Planets VI*, University of Arizona Press, Tucson, p. 267
- Seifried, D., Banerjee, R., Pudritz, R. E., & Klessen, R. S. 2013, *MNRAS*, 432, 3320
- Shu, F. H., Najita, J. R., Shang, H., & Li, Z.-Y. 2000, *Protostars and Planets IV*, p. 789
- Stehle, R., & Spruit, H. C. 2001, *MNRAS*, 323, 587
- Tibbs, C. T., Paladini, R., Cleary, K., Muchovej, S. J. C., Scaife, A. M. M., Stevenson, M. A., Laureijs, R. J., Ysard, N., Grainge, K. J. B., Perrott, Y. C., Rumsey, C., & Villadsen, J. 2015, *MNRAS*, 456, 2290
- Tielens, A. G. G. M., Hagen, W. 1982, *A&A*, 114, 245
- Tobin, J. J., Hartmann, L., Chiang, H.-F., Wilner, D. J., Looney, L. W., Loinard, L., Calvet, N., & D'Alessio, P. 2012, *Nature*, 492, 83
- Tobin, J. J., Hartmann, L., Chiang, H.-F., Wilner, D. J., Looney, L. W., Loinard, L., Calvet, N., & D'Alessio, P. 2013, *ApJ*, 771, 48
- Tobin, J. J., Kratter, K. M., Persson, M. V., Looney, L. W., Dunham, M. M., Segura-Cox, D., Li, Z.-Y., Chandler, C. J., Sadavoy, S. I., Harris, R. J., Melis, C., & Pérez, L. M. 2016, *Nature*, 538, 483
- Tokuda, K., Onishi, T., Saigo, K., Kawamura, A., Fukui, Y., Matsumoto, T., Inutsuka, S., Machida, M. N., Tomida, K., & Tachihara, K. 2014, *ApJ*, 789, 4
- Tomida, K., Tomisaka, K., Matsumoto, T., Hori, Y., Okuzumi, S., Machida, M. N., & Saigo, K. 2013, *ApJ*, 763, 6
- Tomida, K., Okuzumi, S., & Machida, M. N. 2015, *ApJ*, 801, 117
- Toomre, A. 1964, *ApJ*, 139, 1217
- Troland, T. H., & Crutcher R. M. 2008, *ApJ*, 680, 457
- Tsukamoto, Y., Iwasaki, K., Okuzumi, S., Machida, M. N., Inutsuka, S. 2015, *MNRAS*, 452, 278
- Tsukamoto, Y., Iwasaki, K., Okuzumi, S., Machida, M. N., Inutsuka, S. 2015, *ApJ*, 810, 26
- Vorobyov, E. I., & Basu, S. 2006, *ApJ*, 650, 956
- Vorobyov, E. I., & Basu, S. 2015, *ApJ*, 805, 115
- Wurst, J., Price, D. J., & Bate, M. R. 2016, *MNRAS*, 457, 1037
- Wurst, J., Price, D. J., & Bate, M. R. 2017, *MNRAS*, 466, 1788
- Yen, H.-W., Shigehisa T., & Nagayoshi O. 2010, *ApJ*, 710, 1786
- Yen, H.-W., Koch, P. M., Takakuwa, S., Ho, P. T. P., Ohashi, N., & Tang, Y.-W. 2015, *ApJ*, 799, 193
- Yen, H.-W., Takakuwa, S., Koch, P. M., Aso, Y., Koyamatsu, S., Krasnopolsky, R., & Ohashi, N. 2015, *ApJ*, 812, 129
- Yen, H.-W., Takakuwa, S., Chu, Y.-H., Hirano, N., Ho, P. T. P., Kanagawa, K. D., Lee, C.-F., Liu, H. B., Liu, S.-Y., Matsumoto, T., Matsushita, S., Muto, T., Saigo, K., Tang, Y.-W., Trejo, A., & Wu, C.-J. 2017, arXiv:1708.02384
- Zhao, B., Li, Z.-Y., Nakamura, F., Krasnopolsky, R., & Shang, H. 2011, *ApJ*, 742, 10
- Zhao, B., Caselli, P., Li, Z.-Y., Krasnopolsky, R., Shang, H., & Nakamura, F. 2016, *MNRAS*, 111, 22

This paper has been typeset from a  $\text{\LaTeX}$  file prepared by the author.